Master of Science Thesis
VT2024

Diffusion-MRI for Characterisation of Head and Neck Tumours

Assessing Distortion Correction Methods

Minoo Gandomi

Supervisors

Minna Lerner, Ivan A. Rashid, Gabriel Adrian,

Lars E. Olsson and Patrik Brynolfsson

Medical Radiation Physics, Lund
Medical Physics Programme
Faculty of Science
Lund University, Sweden
www.msf.lu.se

Populärvetenskaplig sammanfattning

Varje år diagnostiseras ungefär 1600 personer i Sverige med huvud- och halscancer. De flesta av dessa patienter behandlas med strålbehandling, men tyvärr är prognosen för många ganska dålig. Forskning pågår för att förbättra behandlingen och utveckla mer effektiva sätt att döda tumören, samtidigt som man strävar efter att minimera biverkningarna. Ett sätt att göra detta är att använda avancerade bildtekniker, så som magnetkamera-undersökningar (MR), som kan identifiera områden inom tumören som är resistenta mot behandling och sedan anpassa stråldosen därefter.

Diffusions-MR möjliggör kartläggningen av hur vattenmolekyler rör sig i kroppens vävnader. Det förmedlar information om tumörens mikroskopiska struktur och potentiellt även dess syrenivåer, vilket är viktigt eftersom tumörer med låg syrenivå ofta är mer motståndskraftiga mot strålningen. Om dessa områden kan identifieras kan behandlingen optimeras för varje patient, så att den blir mer effektiv. Med nuvarande tekniker för diffusions-MR blir bilderna i huvud-halsområdet ofta av dålig kvalitet. Detta är på grund av att MR-bilder blir förvrängda när material med olika magnetiska egenskaper ligger nära varandra, så som luft, mjukvävnad och ben. I huvud- halsområdet finns det flera sådana problematiska övergångar, som t.ex. i bihålorna, munhålan och svalget, där mycket vävnad gränsar till luft.

I det här arbetet har olika metoder för att förbättra bildkvaliteten i diffusions-MR-bilder undersökts med syfte att öka användbarheten inom strålbehandling. Två bildtekniker, enkel och segmenterad datainsamling har jämförts. Dessutom har olika tekniker för att korrigera förvrängningarna testats, där bilder tas med förvrängningar i motsatta riktningar för att möjliggöra efterföljande korrigeringar.

Resultaten visar att den segmenterade datainsamlingen är mindre känslig för förvrängningar jämfört med den enkla. Bildkvaliteten förbättrades betydligt med korrigeringsteknikerna, särskilt när mer data från motstående insamlingsriktningar användes. Med dessa förbättringar kunde mer geometriskt korrekta bilder av tumörer och omkringliggande vävnad skapas, vilket är avgörande för att sedan kunna identifiera områden med låg syrenivå inom tumören.

För att utvärdera metoderna genomfördes MR-undersökningar både på fantom (en glasburk fylld med gelatin och luft), och på friska frivilliga. Slutligen testades de mest lovande metoderna på patienter med huvud- halscancer, där kartor över tumörens relativa syrenivå kunde skapas. Kartläggningen av syrenivåerna är inte utvärderad, utan ytterligare validering krävs innan metoderna kan implementeras kliniskt.

Sammanfattningsvis visar arbetet att kvaliteten på diffusions-MR-bilder i huvud- och halsområdet kan förbättras genom användning av segmenterad insamling och ytterligare korrigeringstekniker. Detta kan bidra till att optimera strålbehandlingen för patienter med huvud- och halscancer genom att möjliggöra mer exakt avbildning av tumörernas egenskaper och därmed ytterligare individanpassa behandlingen med förbättrade resultat.

Abstract

Diffusion magnetic resonance imaging (dMRI) in radiotherapy has the potential to facilitate the identification of treatment resistant regions within tumours, such as areas with insufficient oxygen supply. This is particularly interesting in head and neck (H&N) tumours with poor prognosis correlated with unidentified hypoxic areas. However, dMRI is sensitivive to the magnetic susceptibility differences between tissues, particularly when using fast imaging techniques such as echo planar imaging (EPI), which can cause geometric distortions. This problem becomes prominent in the complex H&N anatomy as radiotherapy-MRI applications require high spatial accuracy to ensure safe treatments. There are different methods to minimise the distortions, either using post-processing distortion corrections (such as reverse phase encoding techniques) or optimising the image acquisition by using for example multi-shot EPI instead of the conventional single-shot EPI (ssEPI). This project aims to compare the efficacy of various distortion correction techniques in improving the accuracy and reliability of dMRI data. The goal is to obtain usable diffusion images for further research, particularly in the development of imaging biomarkers, and provide guidance for optimising H&N dMRI protocols by evaluating the results in-vivo.

ssEPI and multiplexed sensitivity encoding (MUSE) were compared, both employing several reversed phase encoding gradient corrections as a pre-processing technique. The directions applied were anterior-posterior (AP), posterior-anterior (PA), right-left (RL), left-right (LR), and combinations of AP/PA and RL/LR. The distortion correction was performed either via the FMRIB Software Library or using an embedded vendor-based correction, which uses less reverse phase encoding information. The results were evaluated in both phantom and healthy volunteers through visual and quantitative assessment. Finally, a method based on previous measurements was tested in two patients and the oxygenation of the tumours were mapped.

The results show that the MUSE sequence is less prone to distortions compared to the ssEPI. The quantitative evaluation showed that the distortion corrections notably improved the geometric accuracy of the images. Corrections with more information in the reverse phase encoding direction yield better results compared to corrections containing less information. The efficacy of the correction depends not only on the sequence, but also the direction of the phase encoding pairs in relation phantom geometry. Post-correction, both ssEPI and MUSE are feasible in-vivo with the best options for phase encoding directions being either AP/PA or all four directions. The four-directional corrections with ssEPI and MUSE appear to perform similarly, although small differences in the pharynx and tongue can be observed. The patient examination produced results similar to those of the healthy volunteer, with the addition of revealing tumour tissue. Oxygen maps were successfully generated, but require additional validation prior to implementation. Furthermore, Multi-shot sequences are sensitive to movements between shots, and the MUSE signal may need to be validated. By addressing distortions, it becomes feasible to advance the development of dependable imaging biomarkers for tumour characterisation in H&N.

In conclusion, MUSE shows reduced susceptibility to distortions compared to ssEPI and yields more accurate corrections in certain areas, particularly along the pharynx. It may be the preferred option when the region of interest neighbours a tissue-air interface. Both sequences, particularly when correcting in AP/PA or all four phase encoding directions, offer viable options for in-vivo imaging, although multi-shot sequences may require additional validation due to potential motion-related inaccuracies.

List of Abbreviations

MRI	*Magnetic resonance imaging*
dMRI	*Diffusion magnetic resonance imaging*
H&N	*Head and neck*
ssEPI	*Single-shot echo planar imaging*
MUSE	*Multiplexed sensitivity encoding*
AP	*Anterior-posterior*
PA	*Posterior-anterior*
RL	*Right-left*
LR	*Left-right*
IVIM	*Intravoxel incoherent motion*
CT	*Computed tomography*
SNR	*Signal-to-noise ratio*
ADC	*Apparent diffusion coefficient*
NEX	*Number of excitations*
FOV	*Field of view*

Contents

1 Introduction

The introduction of magnetic resonance imaging (MRI) revolutionised medical diagnostics and research by offering insights into the structure and function of tissues without the use of ionising radiation. Among its various techniques, diffusion MRI (dMRI) has the ability to probe the microstructural properties of tissues based on the random motion of water molecules. dMRI has applications all over the body and is used to investigate many different types of lesions [1]. One major use is to study different characteristics of tumours in order to optimise cancer treatments [2]. The methods developed in this project will be incorporated in the phase III trial ARTSCAN VI to explore tumour characteristics in head and neck (H&N) cancer patients before, during, and after radiotherapy [3]. For the purpose of ARTSCAN VI, the tumour characteristic of interest is hypoxia, which may be investigated through dMRI. However, when imaging the H&N region, dMRI images often exhibit poor image quality, primarily stemming from artefacts and severe geometric distortions [4, 5].

Artefacts such as geometric distortions are the product of magnetic susceptibilities and choice of imaging technique. The susceptibility differences at tissue interfaces within the H&N anatomy and around the aerodigestive tract give rise to distortions when combined with the fast imaging technique conventionally used for dMRI, echo planar imaging (EPI) [6]. These are key contributors to the pronounced distortions often observed in H&N dMRI [7, 8]. These distortions, while problematic in various applications, become particularly critical when high spatial accuracy is demanded, such as in the context of MRI in radiotherapy for H&N cancer treatment planning [9].

For some types of cancer e.g. prostate and brain, MRI has proven valuable in the radiotherapy treatment workflow [10, 11]. MRI provides images with high soft tissue contrast for target delineation and even functional imaging which makes it possible to predict and monitor treatment response [2]. Different tumour properties such as tissue oxygenation which impact the treatment response can be mapped using dMRI [12]. By integrating MRI into radiotherapy, treatment outcomes can better be controlled and radiation exposure to healthy tissues minimised. In this process, precise delineation of tumour boundaries and adjacent critical structures is crucial, meaning that a key criteria for development of new protocols for radiotherapy is geometric accuracy. For this reason, the geometric distortions prevalent in H&N dMRI often make it a challenging modality, especially for higher magnetic field stregths.

There are several existing strategies to mitigate geometric distortions in dMRI, which tackle the problem through different ways, e.g. during image acquisition or pre-processing [13]. A common solution is to use a dMRI sequence less susceptible to geometric distortions compared to the conventional single-shot EPI (ssEPI). One such alternative being investigated in this project is the multi-shot sequenece multiplexed sensitivity encoding (MUSE) [14]. Another common method for minimising distortions is the reverse phase encoding gradient technique, also referred to as blip-up blip-down. This strategy uses images acquired with the distortions in opposite directions in order to make off-line distortion corrections [15, 16]. While these techniques have been extensively studied for certain anatomical regions e.g. the brain, their efficacy in addressing distortions specific to H&N remains to be studied.

1.1 Aim

The primary objective of this thesis is to compare the results of various distortion correction techniques for dMRI in the H&N area. Combinations of two different sequences, ssEPI and MUSE, with distortion corrections using reverse phase encoding gradients are evaluated. The aim is to obtain geometrically accurate images for the development of imaging biomarkers in dMRI, specifically through intravoxel incoherent motion modelling. This study aspires to provide guidance for optimising clinical H&N dMRI protocols, thereby enhancing the utility of dMRI in radiotherapy planning for cancer patients.

2 Background

2.1 Magnetic Resonance Imaging in Radiotherapy

MRI offers soft-tissue contrast vastly superior to that of other imaging modalities such as computed tomography (CT). The higher soft-tissue contrast facilitates the discernment of contours between tissues and organs. The use of different MRI contrasts can also reveal additional information about the properties of the tissues. The most prominent advantage of using MRI in radiotherapy is the precise identification and delineation of boundaries of risk organs and tumour target volumes [11]. There is a growing interest in incorporating MRI methods in radiotherapy [2]. Currently, the use of MRI-only workflows are rising, where the treatment planning is based on information from MRI, completely without the use of CT [10]. The applications for MRI in radiotherapy are increasing and are expected to increase still, extending into the field of functional MRI to investigate different properties of tumours to facilitate the treatment process. One such tumour property of interest is tissue oxygenation [17].

2.2 Hypoxia and Radiosensitivity

The growth of tumours is often characterised by rapid proliferation, outpacing the development of a proper blood supply and leaving the growing tissue unable to sustain its increasing metabolic demands. This process creates regions with reduced levels of oxygen, a condition known as hypoxia. One consequence of hypoxia is the induction of angiogenesis, a process whereby new blood vessels are formed to compensate for the oxygen deficit [18]. Angiogenesis is an adaptive response to hypoxia, triggered by signaling pathways involving hypoxia-inducible factors and vascular endothelial growth factor. However, the newly formed vessels are often structurally and functionally abnormal, prone to collapse [18]. Furthermore, the rapid proliferation of tumour cells results in increased cell density, and constricting and compressing the blood vessels within the tumour, again compromising blood flow and amplifying the hypoxia. The increased cell density restricts the diffusion of oxygen within the tissue and extracellular space, impeding its reach deeper in the tissue (Fig. 1) [19].

Moreover, hypoxia induces radioresistance. Hypoxic environments disrupt the chemical processes crucial for effective radiation-induced DNA damage and subsequent cell death [20, 21]. In the absence of oxygen, the initial chemical reaction in the DNA strand can

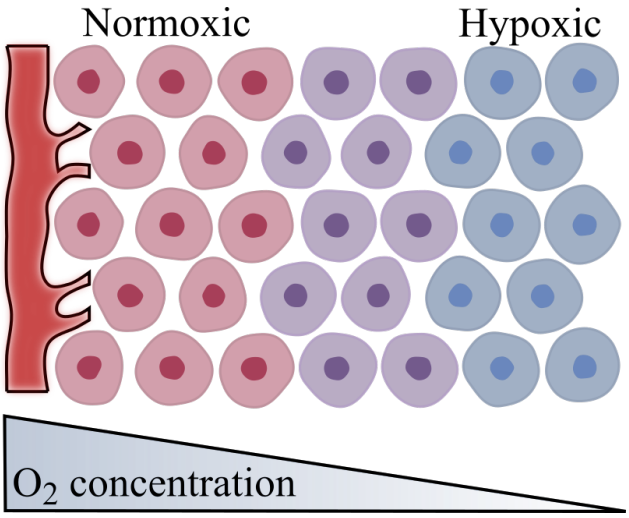

Figure 1: Cells close to blood vessels have a normal oxygen concentration (normoxic), which decreases with increasing distance. Hypoxic cells have a limited oxygen supply.

be reversed, thus preventing damage. When oxygen is present, it acts as an electron donor, thereby fixating the damage and resulting in DNA double-strand breaks. Only after this do the DNA repair mechanisms kick in. Without oxygen fixation, DNA repair mechanisms are considerably more successful and the efficacy of radiation-induced DNA damage in hypoxic environments is reduced. Additionally, hypoxic environments lead to the expression of genes that promote cell survival under stress, influencing metabolism and antioxidant production, helping cells withstand radiation damage [17, 22, 23].

Hypoxia is common in most types of solid tumours, and particularly common in head and neck cancer [24]. Clinically, hypoxic tumours tend to have poor prognosis and be more aggressive [25]. They exhibit heightened resistance to radiotherapy, increased risk of metastasis, lower rates of survival and increased risk of recurrence [21]. As such, hypoxia-induced radioresistance poses challenges in radiation treatment planning and optimisation. Adaptive radiotherapy treatments or dose escalation may have the potential to address these challenges, but require further investigation [20].

Various biomarkers serve as indicators of hypoxia within the tumour and may provide insights into potential radioresistance [21]. Common hypoxia biomarkers include genetic or exogenous markers of cellular oxygenation status, such as staining for hypoxia-inducible factors or pO2-sensitive nitroimidazole compounds (e.g. pimonidazole) [26]. The primary drawback of biopsy-based methods is that the results represent only a small portion of the tumor and lack spatial information. For the purposes of treatment optimisation, there is an interest in determining the oxygen status through imaging techniques.

Several imaging modalities have been proposed for mapping different aspects of hypoxia. Outside of MRI, methods typically use either the PET-tracers ^{18}F-FAZA, ^{18}F-MISO, or dual-CT perfusion [27]. Even within the world of MRI there are several possible methods, e.g. Blood oxygenation level dependent (BOLD) MRI or oxygen-enhanced (OE) MRI. BOLD- or OE-MRI involves supplying the patient with carbogen or oxygen gas and observing the

difference in signal between areas where the oxygen diffuses into the tissue and where it does not [28–30]. In many cases, this can be a bothersome practice. Another method is using dynamic contrast enhanced MRI, which uses an intravenous contrast agent to investigate blood perfusion and cell density [31, 32]. Gadolinium based contrast agents, while often useful, are unfavourable due to potential side effects [33]. Furthermore, patients with reduced kidney function cannot safely be given contrast agent without experiencing side effects [33]. The justification of repeated use of contrast agents has also been discussed due to the fact that the contrast agent remains in some parts of the body e.g. the brain, long after the administration leading to a buildup of gadolinium [34]. For these reasons, there is an interest in developing non-invasive MRI methods to investigate hypoxia without the need for any additional contrasts such as oxygen or gadolinium. One of these methods is intravoxel incoherent motion (IVIM), which uses dMRI to obtain information about the diffusivity and micro-circulation of the tissues [35]. The supply of oxygen is dependent on the capillary network and diffusion through cells in order to reach all areas of tissues. This process in inhibited in areas with high cell density and reduced blood vessels. Hypoxia is then estimated by empirically using maps of the cell density and capillary micro-perfusion and blood volume in the tumour [12].

2.3 Diffusion MRI

Individual molecules suspended in a medium undergo random movement due to collisions and thermal energy, known as Brownian motion. The collective movement due to Brownian motion is known as self-diffusion, not to be confused with the diffusion due to concentration gradients. When unrestricted, the displacement of individual molecules follow a Gaussian distribution if measured along one axis [36]. Otherwise, the diffusion might be dependant on viscosity and temperature of the medium, as well as any obstacles which might restrict the movement of molecules in any direction. As the MRI signals mainly originate from hydrogen nuclei within water molecules, the diffusion of water molecules within water can be measured through dMRI. The high water content in the body allows for biological imaging, where the acquired signal depends on the diffusivity of the imaged tissues. The diffusion within tissues is rarely free, but rather restricted by various micro-, cell- or tissue-structures [37]. There are three different types of diffusion; free, hindered, and restricted. In free diffusion, such as in the cerebrospinal fluid, water molecules are able to move in all directions and their displacement is not impeded by any cellular structures within the medium. Hindered diffusion exists in extracellular space, where water molecules are somewhat limited in their movement. Restricted diffusion occurs when the molecules are contained within a structure, such as a cell, and the movement is restricted to the volume of the structure [36, 37].

2.3.1 Diffusion Weighted Imaging

Diffusion-MRI uses the motion of water molecules in order to create contrast in the images. Based on the measured dMRI signal, and in which directions the diffusion is restricted or free, information about the structures and tissues can be found. This approach utilises diffusion encoding gradients to measure the movement of hydrogen. When a diffusion gradient is applied along an axis the spins experience a spatially varying magnetic field and thus obtain

a difference in Larmor frequency depending on their position along that axis, causing de-phasing. The gradient is then shut off, and a 180 °RF-pulse is applied followed by a gradient in the opposite direction designed to counteract the de-phasing caused by the first gradient [1]. The molecules which remain in the same position throughout this process experience a magnetic field which directly counteracts the effects of the first gradient, which refocuses their spins. Molecules which have moved, i.e. diffused, and are now in a different position do not experience the same field which leads to a Larmor frequency different from that of the first gradient. These spins are not refocused to the same extent. As the MRI signal is dependent on the net spin, diffusion encoding creates contrast in the image based on diffusivity. Tissues with high diffusivity i.e. a lot of movement, result in a lower signal, whereas tissues with low diffusivity and little movement result in higher signal [37]. Furthermore, the signal also depends on the duration of the gradients, the diffusion time, and the gradient amplitude. These parameters are represented by the b-value, which is used to characterise the diffusion gradients [36]. A current clinically used diffusion-based contrast is obtained by calculating the apparent diffusion coefficient (ADC), described by the following:

$$\mathrm{ADC} = \frac{\ln\left(S_0/S(b)\right)}{b} \ , \tag{1}$$

where S_0 and $S(b)$ represent the signal at b-value 0 s/mm^2 and b respectively. Typically, ADC is calculated using a high b-value, around or above 800 s/mm^2 [36]. An ADC map displays the mean diffusion in each voxel, and may show changes in the diffusivity of tissues that appear as a result of lesions.

In order to capture the movement of molecules the imaging technique needs to be fast, as prolonged imaging duration may lead to artefacts and introduce physiological noise due to e.g. breathing or heatbeats [38]. The sequence also needs to have high temporal resolution and low motion motion sensitivity in order to provide accurate results. Therefore, dMRI is commonly performed using EPI sequences

2.3.2 Single- and Multi-shot EPI sequences

Even for EPI sequences there are several possible k-space trajectories and sampling schemes which produces diffusion weighted images. The conventional spin-echo-based ssEPI sequence traverses most or the entirety of k-space in a single shot, acquiring an entire image from each free induction decay. Conversely, the multi-shot sequence uses two or more shots to form one image. Examples of single shot and two types of multi-shot sampling schemes are illustrated in Fig. 2. In ssEPI, all phase-encoding lines are acquired in a single echo train, resulting in rapid image acquisition [39]. This is a highly time efficient method capable of producing large imaging volumes in under a minute. It has become the preferred choice for diffusion imaging primarily because it is largely insensitive to motion, unlike most multi-shot methods. Detecting molecular diffusion on a microscopic scale increases sensitivity to larger movements, such as patient motion. Fortunately, these two types of motion can be somewhat separated in the MRI signal, as diffusion affects the signal magnitude, and patient motion mostly affects signal phase. With ssEPI, the signal phase can be effectively ignored in favour of the magnitude data, reducing the effect of motion artefacts [40]. However, ssEPI

acquisition is more prone to other artefacts and results in lower image quality compared to a conventional spin-echo sequence which reads one phase-encoding line per shot [7]. The sampling requires rapid switching of gradients which induce eddy-currents causing artefacts. All the phase-encoding lines are acquired in a single echo train leading to a low bandwidth in the phase encoding direction and causing signal loss and misplacement [41].

Multi-shot EPI, also referred to as segmented EPI divides the k-space acquisition into multiple segments or shots, each acquiring a subset of the phase-encoding lines [7]. A typical segmented EPI divides the k-space into sections whereby each segment is acquired separately in consecutive shots. The segments then combine to cover the entire k-space, forming one image [39]. The k-space can be segmented in different ways, commonly along the axis of either the phase encoding or frequency encoding direction. Segmentation along the phase encoding direction quickens the time it takes for the readout along that axis, decreasing the effective echo spacing and increasing the bandwidth. Larger bandwidth per pixel allows a larger range of frequencies in each pixel causing less displacement of signal due to field inhomogeneity. Segmented EPI sequences can also be sampled by interleaved read-out of phase-encoding lines. An interleaved EPI acquires the image with shots that are interleaved across k-space, each shot spanning the whole space.

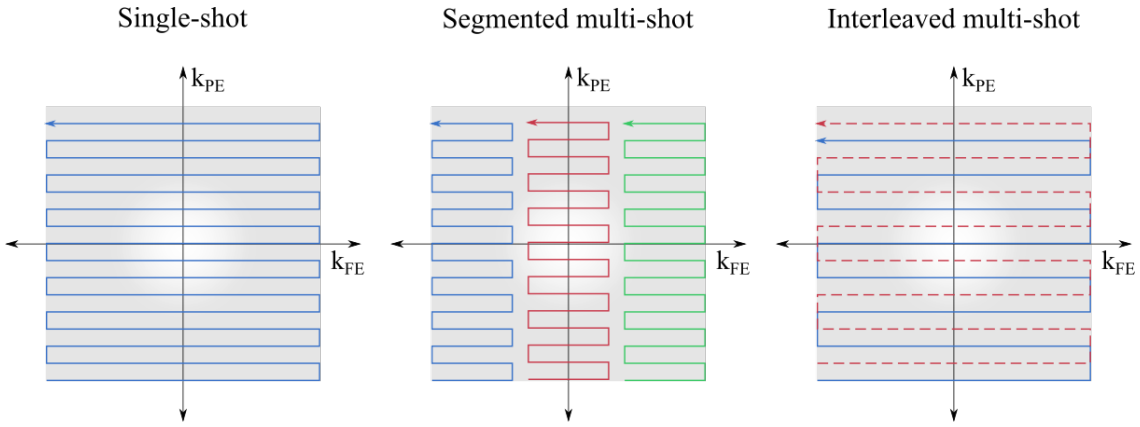

Figure 2: Diagram of the k-space sampling for a single-shot EPI (left) and a three-shot segmented EPI (middle), and an interleaved two-shot EPI (right). k_{PE} and k_{FE} denote the phase and frequency encoding directions respectively.

The multi-shot sequence speeds up the sampling in the phase encoding direction and gives a higher bandwidth which can mitigate some distortions resulting in improved image quality [7]. However, due to the multiple shots spanning the same k-space, multi-shot sequences are particularly sensitive to motions and vibrations. This means that while there are less geometric distortions, there are likely other artefacts. Multiplexed sensitivity encoding (MUSE), a type of interleaved multi-shot sequence, is suggested to mitigate this issue [14, 42]. Compared to other interleaved methods, MUSE is a post-processing technique and does not require any specific hardware or pulse sequence modification. It is based on the SENSE technique, and estimates phase variations between each EPI segment. Unaliased full-FOV images can be estimated from acquired aliased signals using parallel MRI reconstruction. MUSE calculates the magnitude signals of aliased voxels from interleaved EPI segments

using matrix inversion conditioning. The result is an image with fewer artefacts and higher signal-to-noise ratio (SNR) [14].

Ultimately, the quick data acquisition leaves EPI sequences particularly sensitive to susceptibility differences due to the low bandwidth [41]. Furthermore, the addition of the diffusion gradient in the pulse sequence increases the time between the initial excitation pulse to the echo, i.e. the echo time. Longer echo times leave more time for de-phasing of spins, which leads to signal loss. However, the lower limit of the echo time is often dependent on the hardware of the gradient coils. The gradient slew rate plays a crucial role in determining how quickly the phase encoding gradient can be switched, which directly impacts the echo time. This, in combination with the low bandwidth in the phase encoding direction, makes the technique particularly sensitive to magnetic field inhomogeneities causing susceptibility artefacts which geometric distortions. These distortions show up mainly in the phase encoding direction [7].

2.4 Geometric Distortion

The magnetic susceptibility of air is not equal to that of the surrounding tissue. When the magnetic fields are applied across a boundary between air and tissue, the susceptibility difference creates inhomogeneity in the magnetic field, as shown in Fig. 3. There is a difference in magnetic susceptibility between tissue and air. Tissues contain calcium salts and are typically weakly diamagnetic as a result. Air contains mainly oxygen and nitrogen molecules, the former being relatively strongly paramagnetic and the latter being relatively weakly diamagnetic [43]. The result is a slightly paramagnetic gas [8, 44].

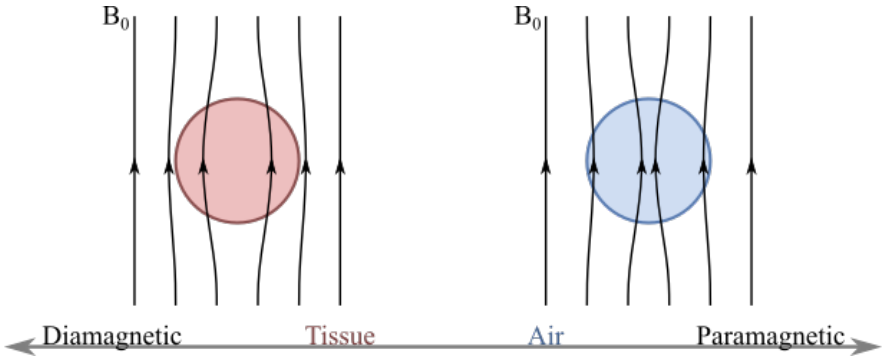

Figure 3: Illustration of the magnetic field lines bending as a result of the magnetic susceptibility of tissue (left) and air (right).

The field inhomogeneities caused by this difference leads to both signal loss and misplacement of signal, so called pile-up. Pile-up is difficult to correct because signal has been accumulated in voxels which do not correspond to the position it originated from, and there is no obvious way to trace the signal back to the voxels where it is supposed to be. These geometric distortions are apparent when imaging the head and neck area, where the aerodigestive tract, sinuses, nasal cavities, and trachea, create large surface interfaces between tissue and air, often decreasing the image quality. The severity of the distortion increases with the magnetic field strength, and is considerably worse for a 3T scanner compared to a 1.5T

scanner [45]. The relationship between the magnitude of distortion, and the magnetic field strength B_0 can be described by:

$$\text{Distortion size} \propto \frac{\Delta\chi \cdot B_0}{BW} \ , \tag{2}$$

where $\Delta\chi$ is the difference in magnetic susceptibility, and BW the bandwidth [45]. The difference in magnetic susceptibility between air and tissue is effectively constant, and the magnetic field strength is determined by the scanner. What remains as a way to reduce the size of susceptibility-based artefacts is the bandwidth, which is determined by the sequence parameters. However, methods using preprocessing techniques may also aid in mitigating geometric distortions.

2.4.1 Distortion Correction

Numerous techniques are available for correcting or compensating for geometric distortions in dMRI. A standard approach involves the utilisation of field maps, wherein a map of magnetic susceptibility is generated to estimate and rectify distortions arising from susceptibility variations. Additionally, registration methods can be used, which may correct distortions through non-rigid registration to a geometrically accurate reference image. Emerging strategies include the application of deep learning algorithms or artificial intelligence. One of the current most common distortion correction techniques is the blip-up blip-down or reverse phase encoding gradients method [13]. The correction works by acquiring two image sets with opposite phase encoding directions. Changing the direction of the phase encoding gradient changes the directions of the artefacts, and allows calculation of a corrected image [15, 41]. Programs using this method are readily available, such as TOPUP (FMRIB Software Library, FSL) [15, 16]. Some manufacturers also have versions already implemented on their systems.

Distortion corrections also come with limitations. Even with the use of correction methods which result in seemingly undistorted images, the signals represented in the voxels have been adjusted during the correction process. While the signal originates from the tissue, the process of correction means that the signal might have been combined or redistributed, leading to potential inaccuracies. Thus, even after correction, the voxel values may not reflect the tissue with complete accuracy. This is an issue with quantitative MRI and dMRI analysis [46]. Models may be very sensitive, and using a quantitative dMRI method on a region which has been corrected may give results with higher uncertainty or bias. In order to minimise the necessity for distortion correction, it is also possible to use a dMRI sequence less susceptible to geometric distortions compared to the conventional EPI sequences. Common alternatives are accelerated variations of the Spin-Echo, such as Turbo-Spin-Echo. The major drawback of this sequence is the long scan time. Examinations of H&N performed using radiotherapy setup tend to be uncomfortable due to the fixation mask ensuring reproducible positioning during imaging and all treatment fractions. Thus, keeping the scan time short is essential for patient comfort and a multi-shot sequence such as MUSE may be a more reasonable alternative.

2.5 The Intravoxel Incoherent Motion Model

IVIM uses dMRI images taken with both high and low b-values in order to estimate not only diffusivity of tissues but also perfusion. Low values are generally considered $b < 200$ s/mm^2 and high values $b > 200$ s/mm^2. The low b-value images taken with weaker diffusion encoding gradients, show signal loss due to both diffusion and micro-circulation [35, 47, 48]. The bi-exponential IVIM model is described by

$$S(b) = S_0 \left[f \ e^{-bD^*} + (1 - f) \ e^{-bD} \right] \ , \tag{3}$$

where $S(b)$ and S_0 are the signal for a given b-value and for b=0 s/mm^2 respectively. Parameters D and f are the diffusion coefficient and perfusion fraction respectively, and relay information about cell density and capillary blood volume. D^* is the pseudo-diffusion coefficient describing the water movement of the blood in capillaries [49]. By taking several images with varying b-values, the signal $S(b)/S_0$ can be plotted and the model fitted similar to Fig. 4. The parameters D, f and D^* can thereby be determined.

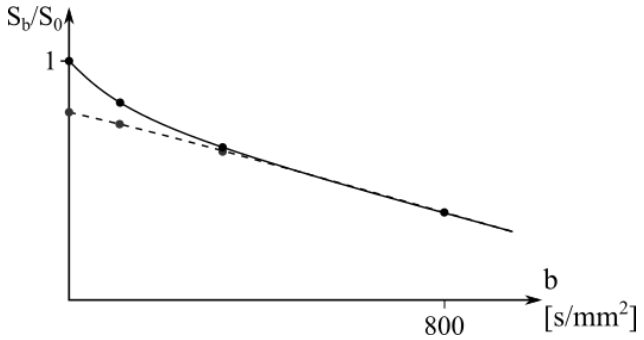

Figure 4: The IVIM model illustrated. The points show $S(b)/S_0$ for each b-value. The difference between the full and dotted line represents the IVIM effect.

IVIM in head and neck cancer has previously been used to investigate different outcome measurements. Several studies show differences in IVIM parameters between benign and malignant tumours, tumour stages, and tumour types [50]. Regardless of outcome measurement, the parameters D and f seem to have the highest predictive value in prognostic studies [50]. The use of IVIM to map hypoxia is a method proposed by Hompland et al, referred to as consumption and supply hypoxia [12]. The method has shown promise in detecting tumour hypoxia in mice, as well as in human prostate and breast [12, 51, 52].

The IVIM model has several inherent challenges which can affect the reliability of its results. Firstly, IVIM functions under the assumption that blood in capillaries move in random directions within the voxel, meaning that the flow in the capillaries change direction several times within the voxel. This may not always be true, particularly in hypoxic areas with collapsed or newly formed blood vessels, impacting the accuracy of the model. Additionally, the IVIM model is highly sensitive to noise, leading to significant uncertainties for high b-value images, especially as the signal approaches the noise floor [35]. Furthermore, the lack of standardised imaging protocol parameters, such as b-values or fitting methods, hinders comparability between studies and sequences. Lastly, the parameter values derived from

the IVIM model, including diffusion coefficient D, perfusion fraction f, and pseudo-diffusion coefficient D^*, may not be directly comparable between different studies or imaging protocol. The parameter values depend not only on the imaged tissue, but also on other parameters of the acquisition, such as magnetic field strength, SNR, the number of b-values and the values chosen, and the IVIM fit used in the analysis [53, 54]. This further complicates the interpretation of results.

Furthermore, the susceptibility difference between tissue and air causes inhomogeneity in all magnetic fields applied across it, even the diffusion gradient. This in combination with other potential inhomogeneities causes background gradients, which lead to inherent variation of b-value in the tissue [55]. This leads to uncertainties in quantitative measurements. A possible way to minimise the effects of background gradients is to collect data using opposite diffusion encoding directions and then take the geometric mean of those directions [56]. For example, rather than only using the directions x, y, and z, their opposite polarity can also be collected, making it x, -x, y, -y, z, -z in total. However this would mean collecting twice as many images and increases the scan time, or dividing the images into twice as many diffusion encoding directions, having a fewer number of excitations per direction.

These challenges need to be carefully considered, and the results validated when applying the IVIM model in clinical research.

3 Materials and Methods

The project was made up of two main parts; phantom measurements and measurements on healthy volunteers, where each step was followed by evaluation of image quality, either quantitative or visual. Following this, the resulting protocol was used to scan two patients. The MRI-scanner used for all measurements was Signa Architect 3T scanner (GE Healthcare, Milwaukee, WI, USA), software version MR30.0_R01, with peak gradient strength 33 mT/m and peak gradient slew rate 120 T/m/s. The imaging protocol was first optimised using the the phantom through repeated measurements and evaluations. The same was then done for in-vivo measurements on healthy volunteers until the resulting images were deemed adequate and a viable protocol for patient imaging was established.

3.1 Phantom Measurements

To begin, the phantom was constructed to mimic head and neck anatomy in order to facilitate the evaluation and optimisation of the imaging protocol.

3.1.1 Construction of the Phantom

The following materials were used during the phantom construction:

- 1.7 L glass jar with accompanying plastic and silicone lid (IKEA), used as the main body of the phantom
- VWR scale

- IKA C-MAG HS 7 control hot plate with accompanying thermometer and magnet stirrer
- Porcine gelatine powder (gel strength 300, type A)
- 10 mM $1 \cdot 10^{-5}$ mol/cm^3 Nickel solution
- Glass test tube 8.5 cm$\times$2 cm
- Glass test tube 17 cm$\times$2 cm
- 1600 mL glass beaker
- 100 mL measuring cylinder

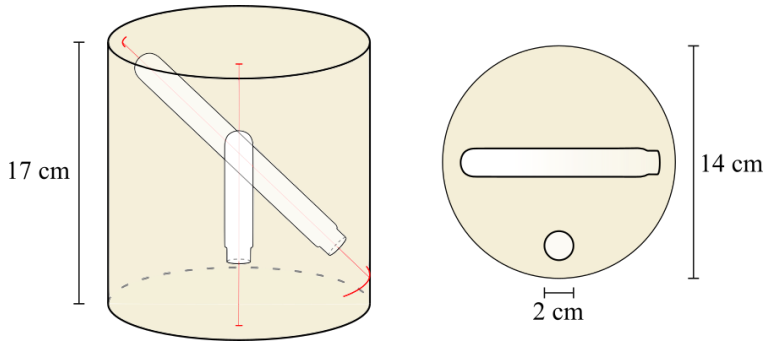

Figure 5: An Illustration of the gel-filled phantom with two empty test tubes used for evaluating geometric distortions. The phantom is illustrated as seen from the side (left) and from above (right).

Using a VWR scale, 1000 g of distilled water was measured and poured into a 1600 mL beaker. The beaker was placed on a hotplate (IKA C-MAG HS 7 control). The accompanying thermometer and a large magnetic stirrer were placed into the beaker. 80 g of gelatin from porcine skin (gel strength 300, type A) was measured using the aforementioned scale. The magnetic spinning was started with 70 rmp and around 1/4 or the gelatin powder was dusted over the water in the beaker. Once the gelatin started sinking into the water, the rest of the gelatin powder was dusted on top and the spinning increased to 200 rpm. Once all of the powder had been saturated by the water the hotplate was turned on to 50 °C, and the spin increased to 380 rpm. The mixture was left to dissolve. Once dissolved, the spinning was gradually decreased 70 rpm to prevent bubbles or excess foam to form. After reaching 50 °C, the heat was turned off to allow the mixture to cool. 60 mL of diluted Nickel (10 mM $1 \cdot 10^{-5}$ mol/cm^3) was measured in a 100 mL measuring cylinder. When the mixture had cooled to 40 °C, the Nickel solution was mixed in. The gelatin mix was then poured into the 1.7 L glass jar until the layer was approximately 7 cm thick. The glass jar was then placed into a refrigerator, and the beaker containing the remaining gelatin mixture was covered with a lid and left in room

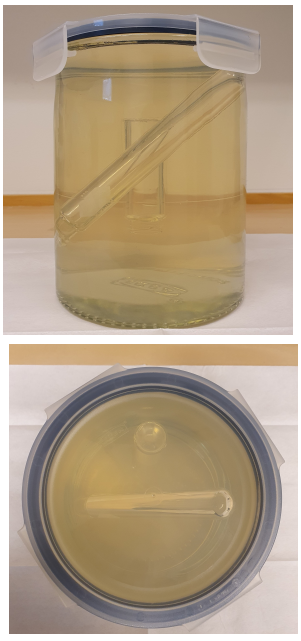

Figure 6: The phantom as seen from the side and above.

temperature for approximately 1 h. This allowed the gelatin in the
jar to set while the one in the beaker remained fluid albeit thick. The jar was then brought out of the refrigerator. Another layer of gelatin mixture was poured in the jar on top of the cold gelatin, approximately 5 cm thick. The two test tubes were lowered into the still-fluid gelatin in the jar and manually held in place according to Fig. 5 for approximately 10 minutes while the surrounding gelatin set. The remaining gelatin mixture in the beaker was then poured on top and the jar was once again placed in the refrigerator. Another batch of gelatin mixture was created according to the above method. The mixture was poured in the jar until the jar was full. The jar was once again placed in the refrigerator. The gelatin mixture in the beaker was also poured into the lid of the jar and left to cool in the refrigerator. Once the gelatin in the lid had begun to set in the lid, the lid was carefully placed on top of the jar and secured. The complete phantom was put in the refrigerator for final storage. The result is seen in Fig. 6.

3.1.2 Phantom Imaging Protocol

During the image optimisation process, adjustments were made in matrix size, FOV, number of excitations, number of shots, and different vendor-based image corrections and algorithms. The method described in this section is the final method used to produce the results seen in following sections. Ten images were produced using a combination of the two sequences and different corrections methods.

The phantom was scanned using a 30-channel flex coil and the embedded 40-channel posterior array coil. Imaging was first performed using an ssEPI sequence with varying number of excitations (NEX) for the phase encoding directions. Different NEX (2,4,8) and four different phase encoding directions, anterior-posterior (AP), posterior-anterior (PA), right-left (RL), and left-right (LR), as described in Tab. 1 were set consecutively. The NEX=8 distortion correction was performed using the embedded vendor implementation which uses only one additional b0 image with the opposite phase encoding polarity. The remaining corrections were performed using TOPUP (FMRIB Software Library, FSL) [15, 16]. The NEX=4 was used for distortion correction in two directions, AP/PA or RL/LR separately. NEX=2 was used to correct with all four phase encoding directions simultaneously. This way the SNR and scan time were comparable for all distortion corrected images. The ssEPI imaging used a vendor-based deep-learning SNR improving algorithm in the reconstruction (AIR™Recon DL). The effective echo spacing for the ssEPI sequence was 0.744 ms.

Imaging was then performed using the multi-shot sequence MUSE, with three shots. Data collection was similar to that of ssEPI, but with NEX=1, 2, and 4 as outlined in Tab. 1. NEX=4 was used for the vendor-specific correction, and the remaining images were corrected using TOPUP. The MUSE images were not reconstructed using any SNR improving algorithm as it was incompatible with the sequence. The voxel size was set to $2\times2\times4$ mm^3, matrix size 108×108, 220×220 mm^2 FOV, 30 slices, echo time 70.9 ms, and four b-values were selected (0, 50, 200, 800) s/mm^2. The effective echo spacing for MUSE was 0.247 ms. A T2w image was acquired as a reference for geometric accuracy using a fast spin echo sequence.

Table 1: Imaging parameters and correction methods for the ten phantom images. The total scan time is the combined scan time for the images taken with the specified phase encoding directions.

Sequence	NEX	Phase Encoding Directions	Correction method	Total scan time
ssEPI	8	AP + PA (b0 only)	Vendor	5 min 15 s
		RL + LR (b0 only)	Vendor	5 min 15 s
	4	AP + PA	TOPUP	5 min 17 s
		RL + LR	TOPUP	5 min 17 s
	2	AP + PA + RL + LR	TOPUP	5 min 19 s
MUSE	4	AP + PA (b0 only)	Vendor	7 min 19 s
		RL + LR (b0 only)	Vendor	7 min 19 s
	2	AP + PA	TOPUP	7 min 22 s
		RL + LR	TOPUP	7 min 22 s
	1	AP + PA + RL + LR	TOPUP	7 min 24 s

3.1.3 Evaluation of Phantom Images

The phantom images were evaluated both visually and quantitatively using the software platform Hero Imaging (Hero Imaging AB, Umeå, Sweden). The T2w image was used as the geometrically accurate ground truth. For the quantitative evaluation, the images were registered to the T2w image using a rigid registration (Elastix) [57]. Masks of the diffusion images were created using thresholding (values ¿ 2400) followed by the morphological operation opening. Three contour structures were then outlined from each of the ten b0 masks, each contour corresponding to the interfaces in the phantom (see Fig. 7). The contours were filled in, converting them to volumes. The three volume structures were evaluated separately. Thirteen slices across the phantom which contained both test tubes and thus all three outline structures were used. For each diffusion image, the three structures of the b0 image was compared to the T2w image by Dice coefficient and average Hausdorff distance. The Dice similarity coefficient for binary data is defined by

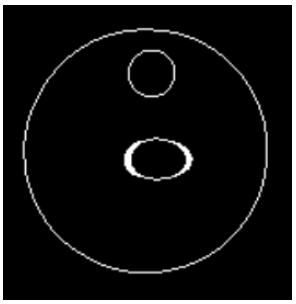

Figure 7: The three structures of the phantom, the outer surface, the upper circle and the centre oval. The contours were filled in for the quantitative evaluation.

$$DSC = \frac{2 \cdot TP}{2 \cdot TP + FP + FN} \ , \tag{4}$$

where true positive TP represents the true values overlapping between the T2 and the diffusion binary masks, false positive FP the true values in the diffusion masks which are false in the T2 mask, and false negative FN the values which are true in the T2 mask but false in the diffusion masks. The result is a fraction between 0 and 1 where 1 implies perfect agreement.

The average Hausdorff distance was used as a metric for how far the values in the diffusion masks lie from the T2 mask. The Hausdorff distance between two subsets A and B is given

by,

$$\mathrm{d}_H(A,B) = \max\left\{\sup_{a\in A}\inf_{b\in B} d(a,b), \sup_{b\in B}\inf_{a\in A} d(a,b)\right\} \ , \tag{5}$$

where sup and inf represent the supremum and infimum operator respectively. Essentially, the metric measures the greatest distance from any point in one set to the nearest point in the other set. If every point in the two sets overlap the distance is zero. Since it measures the maximum distance, the metric is sensitive to outliers. The Average Hausdorff distance averages the minimum distances rather than taking the maximum, and is less sensitive to outliers. The results of these metrics were used as foundation for the in-vivo protocol.

In order to investigate the effect of susceptibility differences on the diffusion encoding gradient, the phantom was imaged with a separate sequence in diffusion encoding directions (x, -x, y, -y, z, -z) for b=800 s/mm^2, with one extraction per direction. The remaining parameters were identical to those of the phantom imaging protocol. The ADC was then calculated using b=0 and b=800 s/mm^2 with three directions (x, y, z), and all six directions respectively and the two results were compared visually.

3.2 In-vivo Measurements

3.2.1 In-vivo Imaging Protocol

The in-vivo imaging was performed on a healthy volunteer. The initial protocol, prior to optimisation, was a ssEPI sequence with echo time 73.7 ms, voxel size 1.5×1.5×3 mm^3, matrix size 166×166, 250×250 mm^2 FOV. The effective echo spacing for the initial imaging was 0.864 ms. Standard fat suppression was selected and images with the phase encoding directions AP, PA, RL, and LR were acquired. The protocol was the optimised through an iterative process interleaved with the phantom measurements, where parameters were adjusted after repeated measurements and evaluations. The resultant imaging protocol, post optimisation, is outlined in Tab. 2. Imaging was performed with a radiotherapy coil setup (see Fig. 8), using two 6-channel and one 16-channel flex coil, as well as the open panel 8-channel coil, with the above sequences and CHESS fat suppression. Voxel size was set to 2×2×4 mm^3, matrix size 108×108, 220×220 mm^2 FOV, 30 slices, echo time 70.9 ms, and four b-values were selected (0, 50, 200, 800) s/mm^2. A T2w image was acquired as a geometrically accurate reference. The effective echo spacing was 0.744 ms for ssEPI and 0.245 ms for MUSE.

Figure 8: The setup of a healthy volunteer, showing the flex coils attached to either side of the head and across the body and neck.

Table 2: Imaging parameters and correction methods for the in-vivo images. The total scan time is the combined scan time for the images taken with the specified phase encoding directions. The increased scan time is due to the selected enhanced fat suppression.

Sequence	NEX	Phase Encoding Directions	Correction method	Total scan time
ssEPI	4	AP + PA	TOPUP	5 min 40 s
	2	AP + PA + RL + LR	TOPUP	5 min 42 s
MUSE	1	AP + PA + RL + LR	TOPUP	8 min 36 s

3.2.2 In-vivo Evaluation and Patient Measurements

The in-vivo images were evaluated visually between five medical physicists and one oncologist. Warpfield images were generated through the TOPUP algorithm to show the displacement (mm) of the correction. This was done in order to indicate the uncertainly in the signal values. Furthermore, the b=800 s/mm^2 images were averaged as a way to visually compare the SNR. Based on the evaluation, the ssEPI in AP+PA and MUSE in all four directions were finally used for patient scans. The patients were scanned in a coil setup identical to the healthy volunteers, and instructed to refrain from swallowing except between sequences. Prior to the examination, informed consent was obtained from both healthy volunteers and patients. Examinations were approved by the Regional Ethical Review Board in Lund, Sweden (Dnr 2020-06389, Dnr 2023-04751).

Two patients were examined using the protocol. Patient 1 was a 68-year-old male with squamous cell carcinoma of the tonsils, stage T4N1, planned to be treated with radiotherapy (68 Gy/34 fractions). The gross tumour volume of patient 1 was 30.2 cm^3. Patient 2 was examined wearing a radiotherapy mask and dental guard. The patient was a 65-year-old male, with squamous cell carcinoma of the tonsils, stage T4N1, and was a study patient in ARTSCAN VI intended for radiotherapy up to 83 Gy to a gross tumour volume of 48.7 cm^3.

3.2.3 IVIM Analysis

IVIM was calculated on the gross target volume for the two patients. The diffusion images were first registered to their respective b0 image. The b0 image was then registered to the

T2w image. The transformation between b0 and T2W image was applied to the rest of the diffusion images. The images were averaged for each b-value and a mask around the outer surface of the body was applied. A simplified mono-exponential model (Eq. 6) was applied using $b = (0, 200, 800)$ s/mm^2,

$$S(b) = S_0 \left[(1 - f) \cdot e^{-bD}\right] \tag{6}$$

where D was obtained by fitting of high b-values $b = (200, 800)$ s/mm^2, and f was found by extrapolating the fitted curve to the $b = 0$ s/mm^2 intercept. The simplified model was chosen for robustness rather than accuracy. As the direct results of these maps was not intended to be used clinically, the choice of IVIM model was not optimised. Consumption and supply based hypoxia was mapped based on IVIM parameter maps using the method described in Hompland et al [12]. The method uses a linear fit of f against D to discriminate hypoxic voxels from non-hypoxic voxels, where voxels with low D and f correspond to hypoxic areas. The gross tumour volume contour structure was imported from a previous CT examination, registered into the T2w space, and transformed to a mask. The tumour mask was applied to the IVIM parameter maps and hypoxia map. The tumour maps for f, D, and hypoxia were overlaid the T2w image.

4 Results

4.1 Phantom Images

The results of the four different phase encoding directions for both sequences, ssEPI and MUSE, are shown in Fig. 9 and 10 respectively. The two sequences produce similar susceptibility artefacts, albeit to varying degrees, with ssEPI exhibiting greater susceptibility artifacts compared to MUSE. The distortions differ between the two test tubes within the phantom. The longer test tube, positioned diagonally across the phantom and appearing as an oval in the centre, exhibits severe distortions. Conversely, the shorter test tube, aligned parallel to the phantom and presenting as a circle at the top, shows less distortion. The circular shape shows varying degrees of distortion with some signal misplacement in the phase encoding direction. In the case of AP phase encoding, this results in darker areas on the anterior side of the circle and lighter areas on the posterior side.

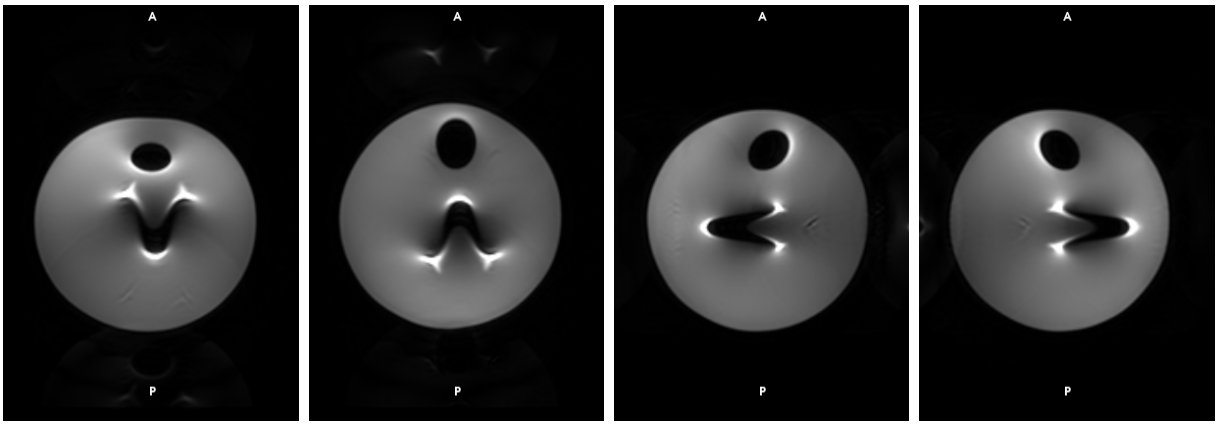

Figure 9: Axial phantom $b0$ images taken with ssEPI in the phase encoding directions AP, PA, RL, LR from left to right.

The MUSE images (Fig. 10) are less distorted and have less pile-up particularly around the circle. Some other artefacts are visible.

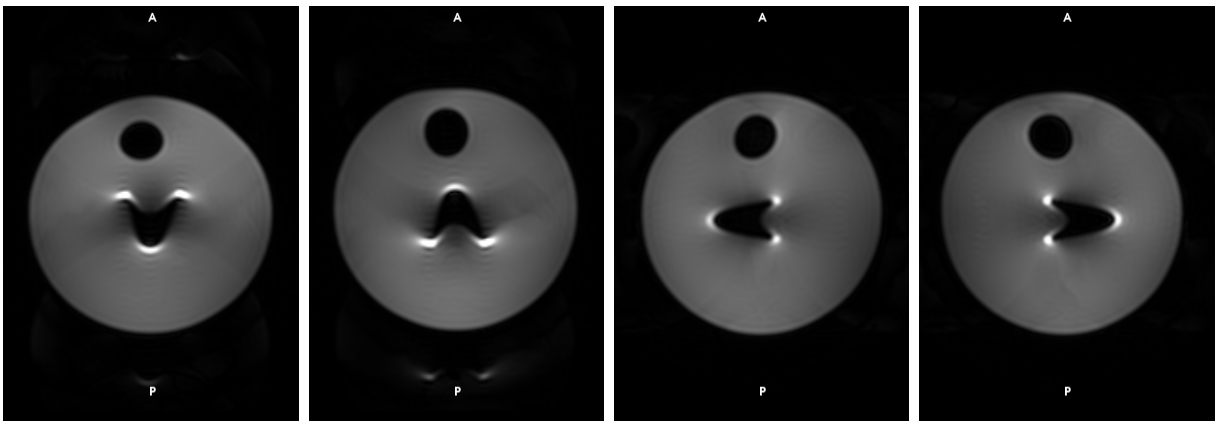

Figure 10: Axial phantom $b0$ images taken with MUSE in the phase encoding directions AP, PA, RL, LR from left to right.

Each sequence was corrected using four different methods (Tab. 1), presented in Figs. 11 and 12. The MUSE images had less pile-up and were more homogeneous after correction. The shape of the body of the phantom is corrected well in every correction for every sequence.

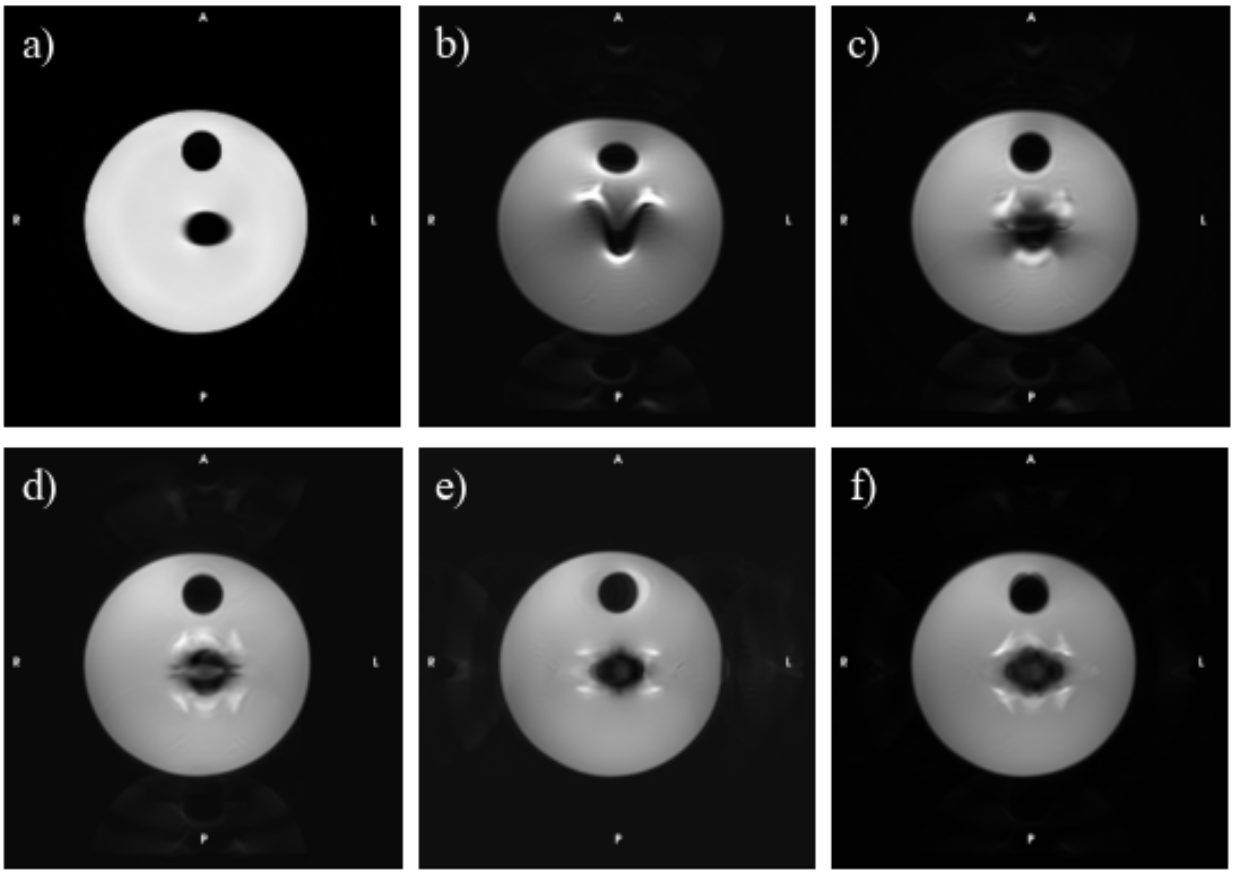

Figure 11: Axial reference and ssEPI phantom $b0$ images corrected using different methods and datasets; a) T2w b) Original with phase encoding direction AP c) Vendor-corrected in AP/PA d) TOPUP corrected in AP/PA e) TOPUP corrected in RL/LR f) TOPUP corrected in all four directions.

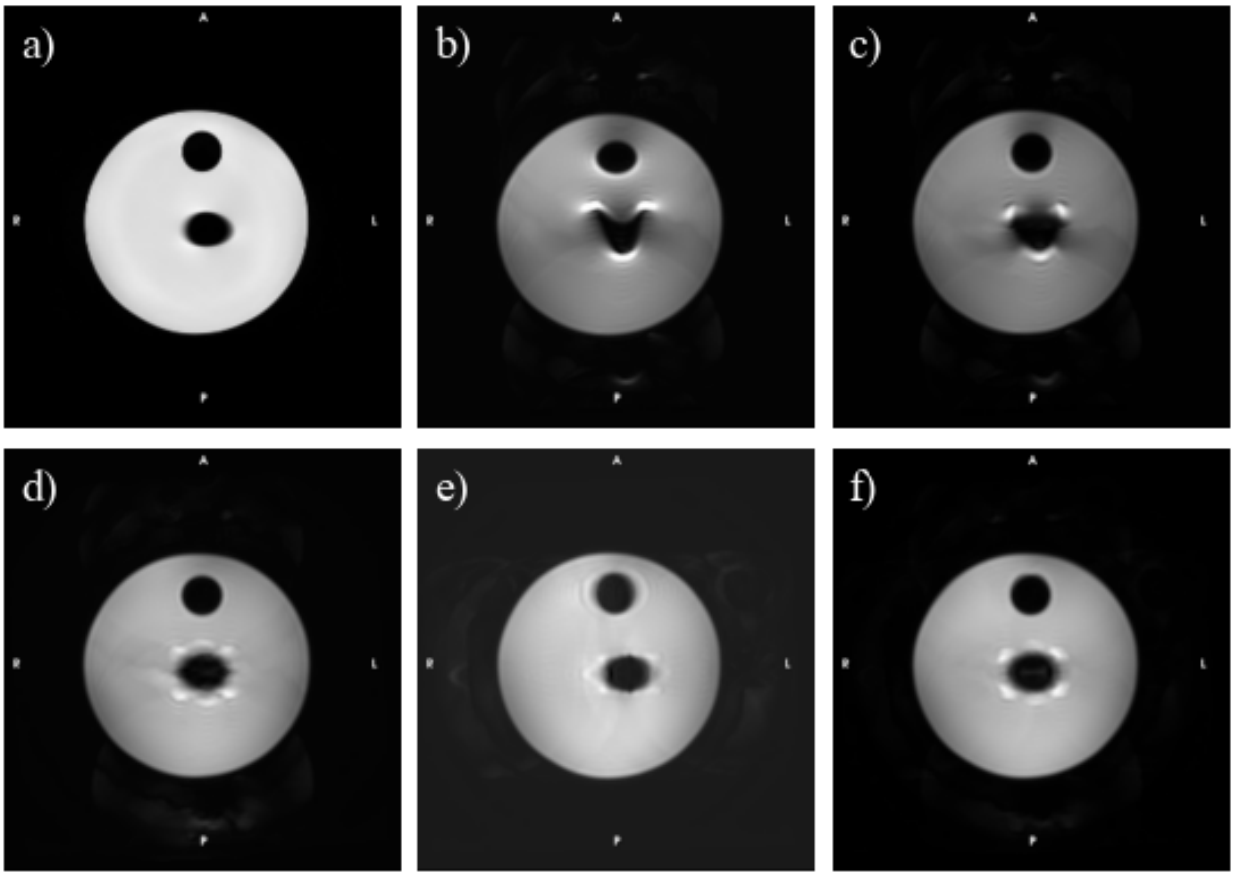

Figure 12: Axial reference and MUSE phantom $b0$ images corrected using different methods and datasets; a) T2w b) Original with phase encoding direction AP c) Vendor-corrected in AP/PA d) TOPUP corrected in AP/PA e) TOPUP corrected in RL/LR f) TOPUP corrected in all four directions.

The uncorrected phantom images (Fig. 11b and 12b), show that the MUSE images have less severe distortions. The body of the phantom is less deformed, and the central oval is less stretched and has less pile-up.

The Dice coefficients are shown in Fig. 13 and 14. The MUSE images have higher score overall, but there is also a large variety depending on the phase encoding directions. The MUSE image corrected in RL/LR shows considerably worse agreement to the T2w image, specifically for the oval, compared to the MUSE AP/PA. The two images with the lowest coefficients are the original ssEPI and MUSE images. The best score is MUSE corrected in AP/PA direction.

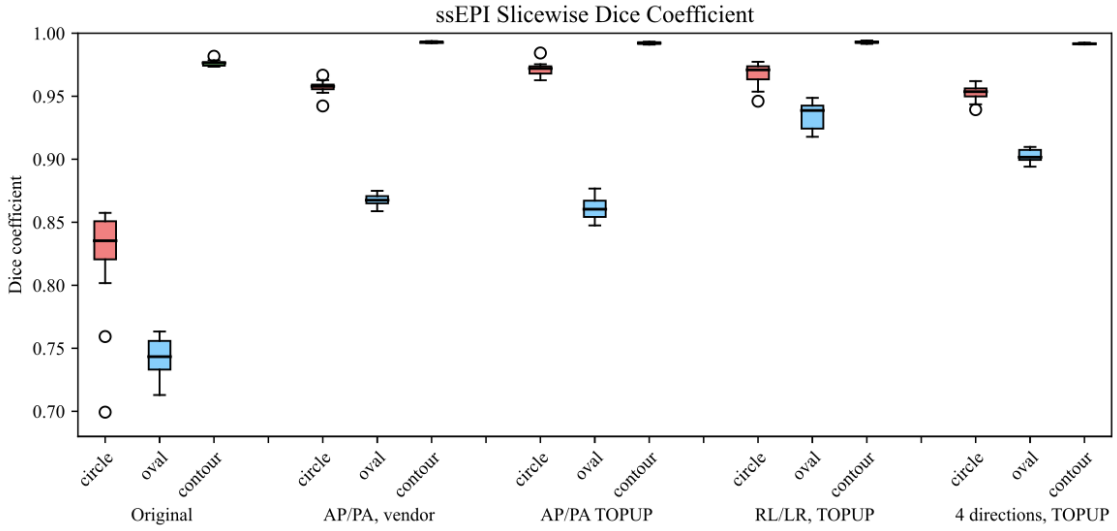

Figure 13: Slicewise Dice coefficients of the ssEPI images from thirteen slices across the centre of the phantom. The three structures, circle (red), oval (blue), and outer surface (green), are described in Fig. 7.

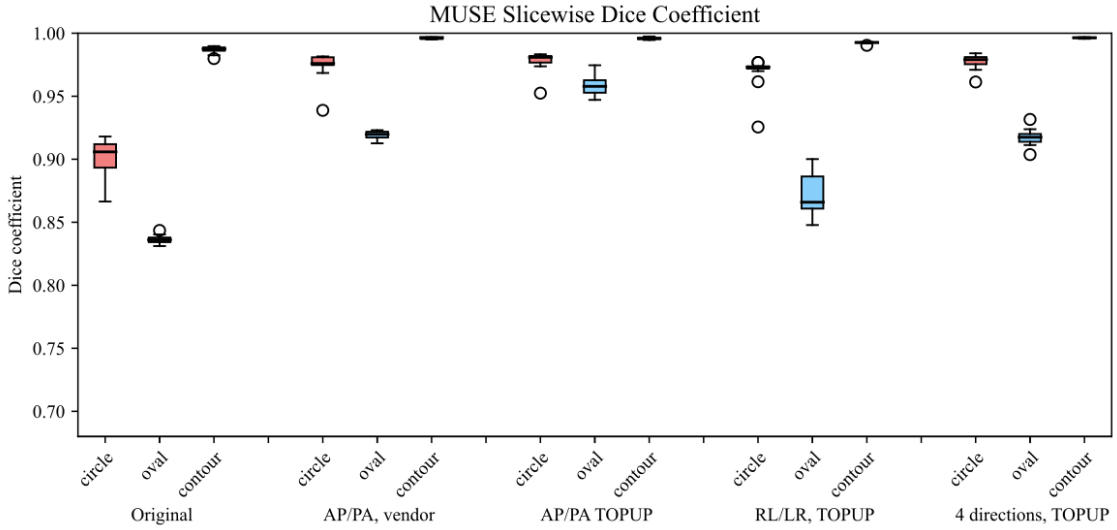

Figure 14: Slicewise Dice coefficients of the MUSE images from thirteen slices across the centre of the phantom. The three structures, circle (red), oval (blue), and outer surface (green), are described in Fig. 7.

The average Hausdorff distance for the images is shown in Fig. 15 and 16. The image with the worst agreement to the T2w is the original ssEPI. Again, the MUSE corrected in RL/LR has a comparatively high average Hausdorff distance for the oval structure. The corrected MUSE image in AP/PA has the best agreement.

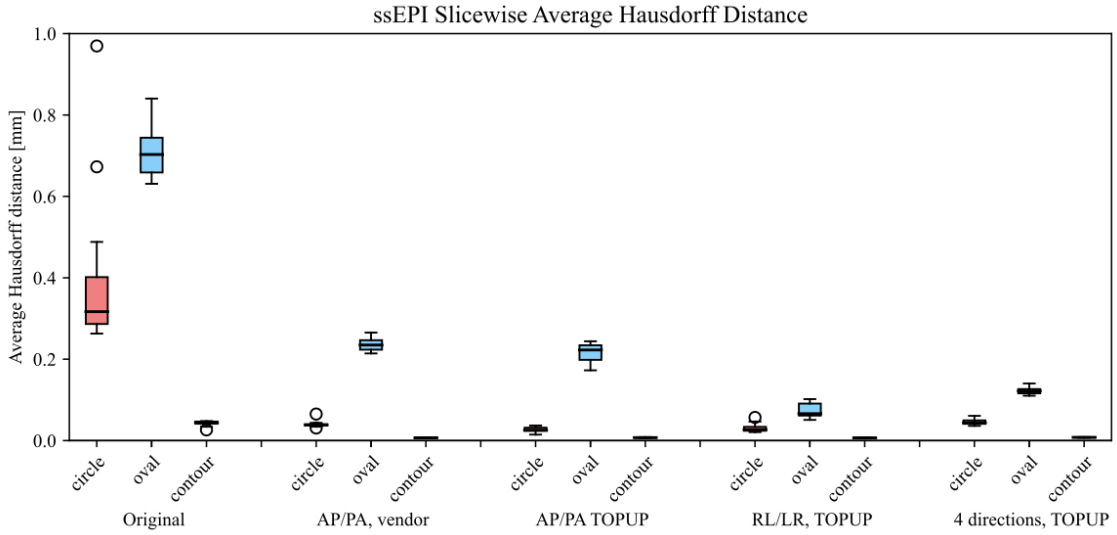

Figure 15: Slicewise average Hausdorff distance of the ssEPI images from thirteen slices across the centre of the phantom. The three structures, circle (red), oval (blue), and outer surface (green), are described in Fig. 7.

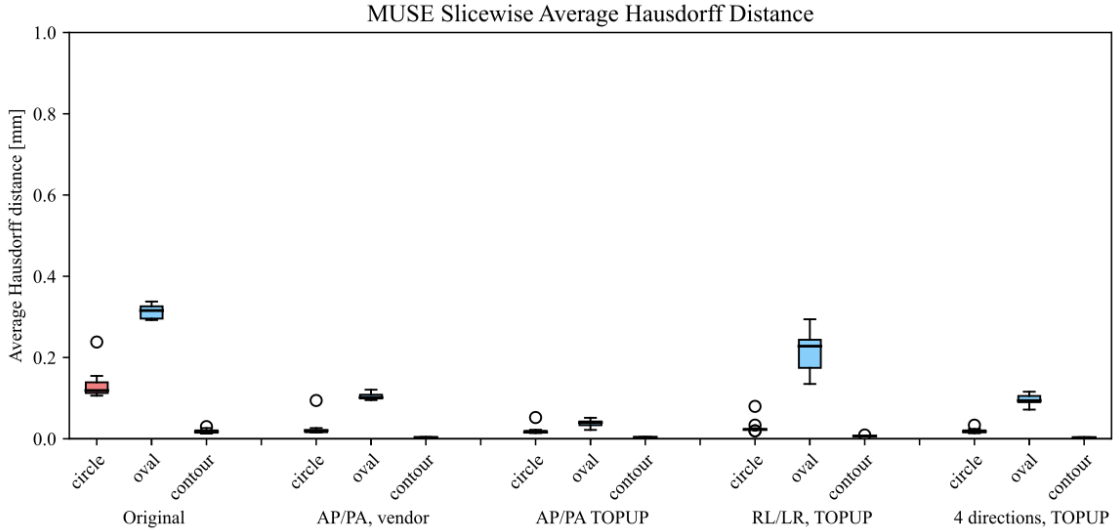

Figure 16: Slicewise average Hausdorff distance of the MUSE images from thirteen slices across the centre of the phantom. The three structures, circle (red), oval (blue), and outer surface (green), are described in Fig. 7.

The effect of background gradients on the ADC can be seen in Fig. 17. The image to the left calculated with only three directions is less homogeneous with lighter and darker areas compared to the one calculated from six directions. All other images obtained in this project were taken using only three orthogonal directions. Any application of this correction was considered a future prospect for this project, and was not included in any in-vivo measurements.

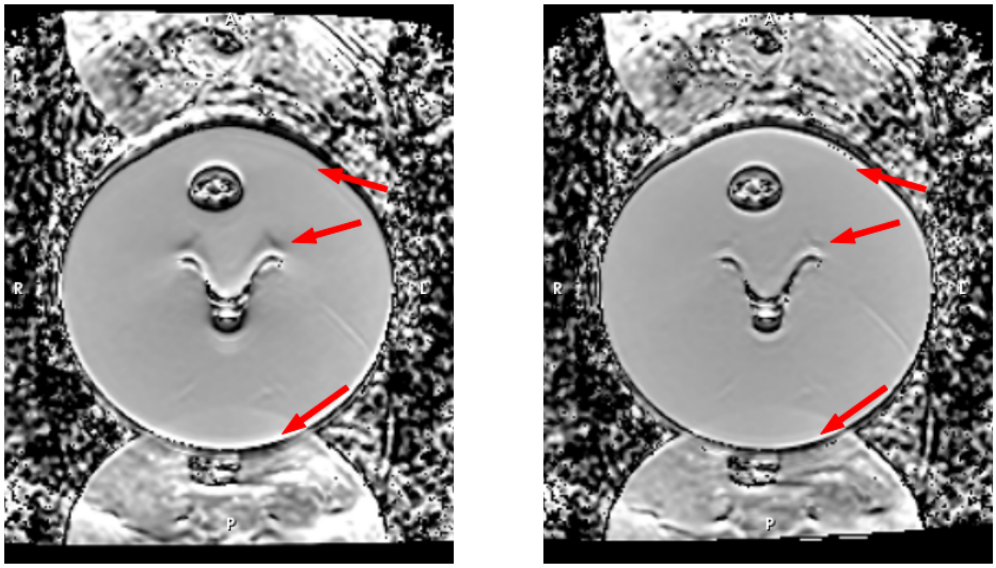

Figure 17: ADC for a ssEPI sequence calculated with diffusion directions x,y,z (left) and x,y,z,-x,-y,-z (right).

4.2 In-vivo Images

4.2.1 Healthy Volunteer Images

The in-vivo images taken with the initial parameters have severe susceptibility artefacts with anatomical features being indistinct and overlapping. In the body, tissue has been more or less distorted leading to areas of tissue, particularly in the anterior, which seem disconnected from the rest of the structure. In the image with direction LR in Fig. 18 there is a section of tissue to the right of the body, which does not appear fully connected to the rest body.

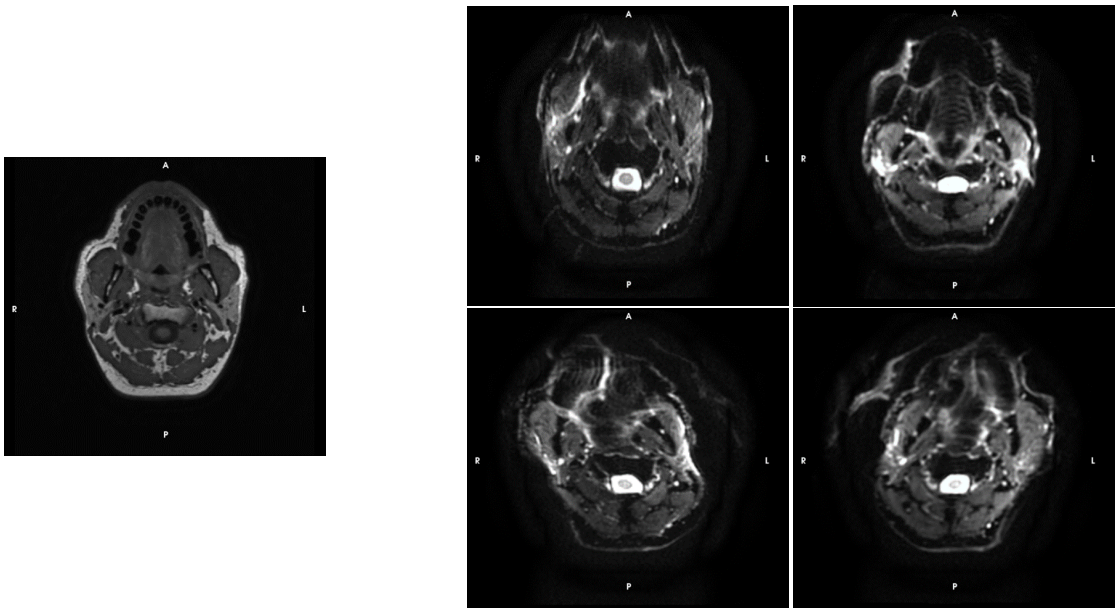

Figure 18: Example in-vivo $b = 0$ images of initial parameters prior to optimisation or correction. T1w image (left), and four dMRI images to the right, taken with ssEPI and phase encoding directions AP, PA, RL, LR respectively.

The images in Fig. 19 show the directions AP and RL for ssEPI and MUSE. The distortions are less severe, albeit still evident. The RL images are stretched to the left, more so in the ssEPI image. The corrected images all seem to match well with the T2w image. The biggest difference between the images can be seen in the area around the pharynx, as indicated by the red arrow in the images.

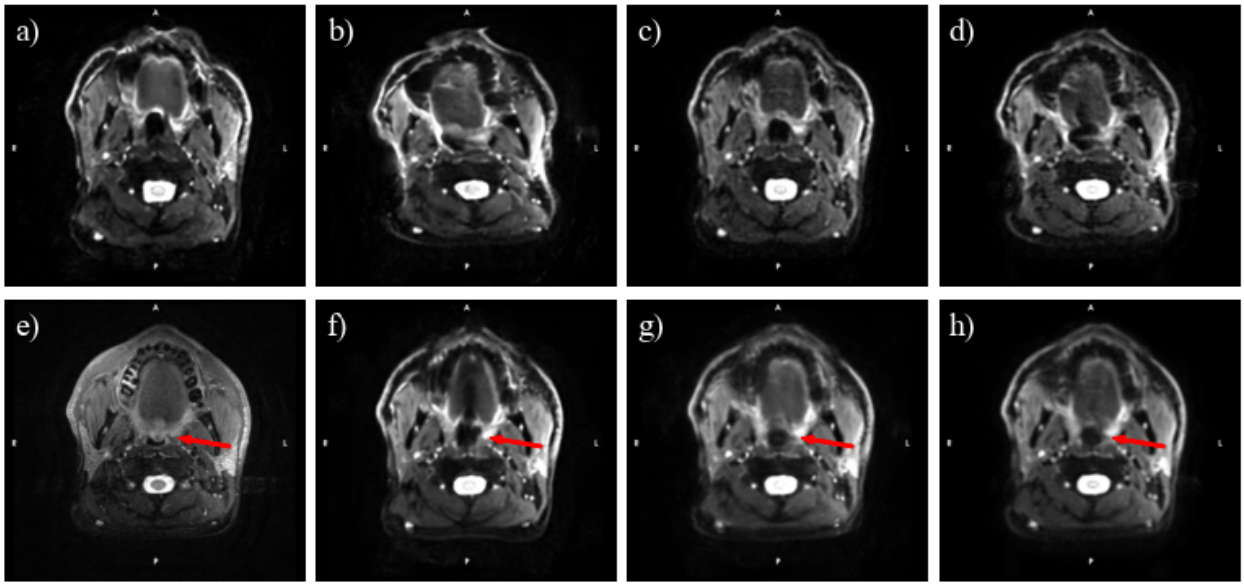

Figure 19: In-vivo $b = 0$ images of a healthy volunteer with original uncorrected images on the top row, and a T2w image and corrected images on the bottom row. a) Original ssEPI in AP b) Original ssEPI in RL c) Original MUSE in AP d) Original MUSE in RL e) T2w f) TOPUP corrected ssEPI in AP/PA g) TOPUP corrected ssEPI in four directions h) TOPUP corrected MUSE in four directions. The arrows indicate the oropharynx.

The displacement maps (Fig. 20) show that the ssEPI has a generally larger displacement compared to MUSE.

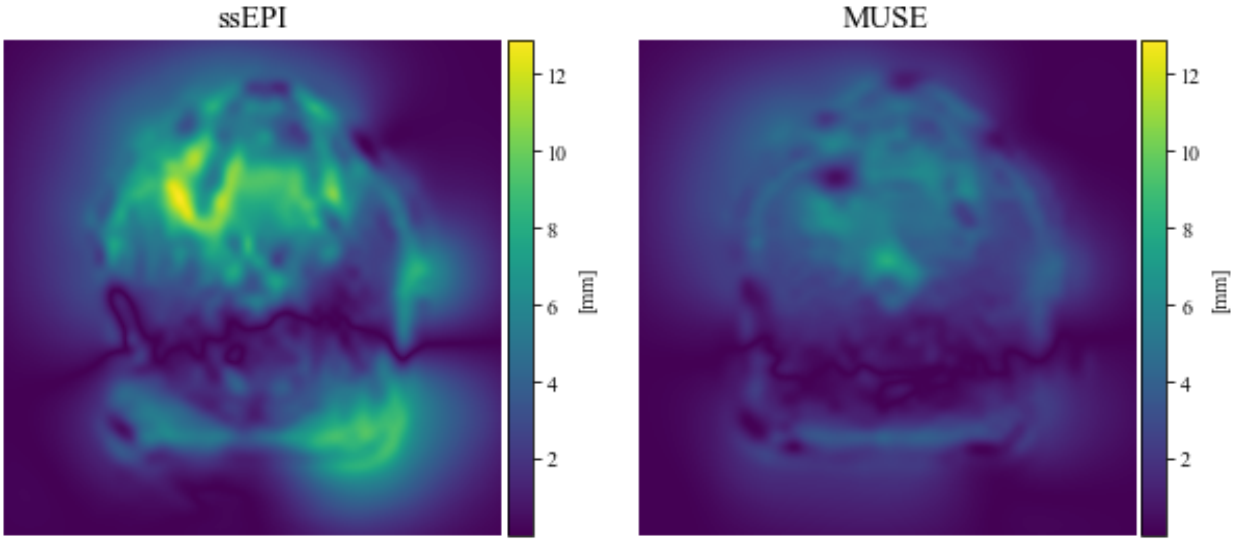

Figure 20: Displacement maps (in mm) of the healthy volunteer. ssEPI is in AP/PA is shown to the left and MUSE in all four directions to the right.

The b800 images from ssEPI and MUSE (Fig. 21) show that the ssEPI has a higher SNR and a smoother appearance compared to MUSE. This is likely attributed to the vendor-based SNR improving algorithm used for ssEPI only.

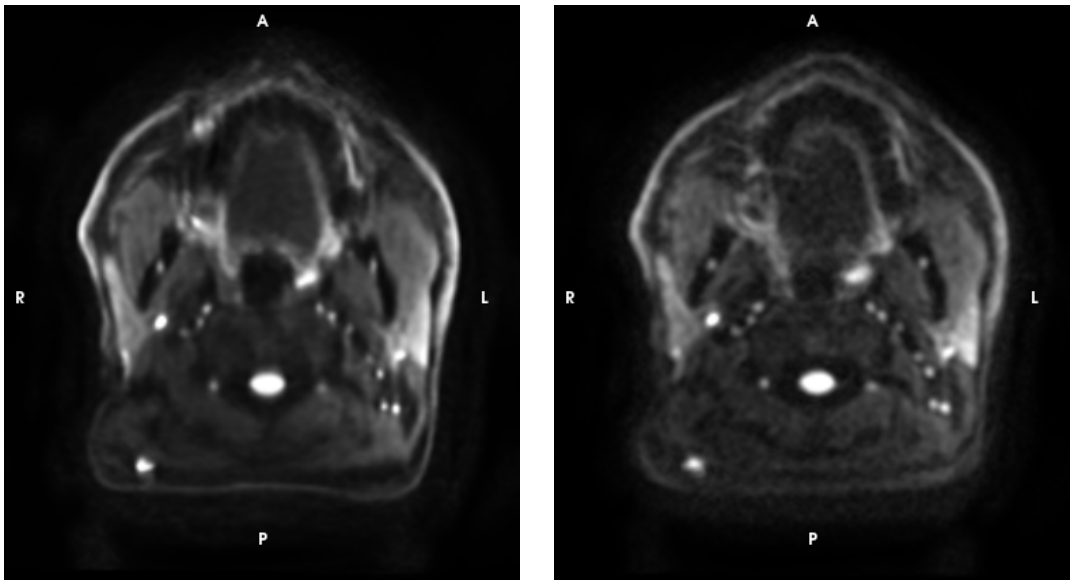

Figure 21: Averaged diffusion images of a healthy volunteer with b800 for ssEPI (left) and MUSE(right).

4.2.2 Patient Images

The distortions in the ssEPI patient images (Fig. 22) are very noticeable. The body in the AP image is considerably larger and stretched vertically, whereas the PA direction is compressed. The tumour tissue of the primary tumour is notably distorted in these images. The dental implants also contribute to the distortions, and appear close to the tumour in the PA image. The MUSE images (Fig. 23) show similar characteristics and appearance, but the distortions are less pronounced.

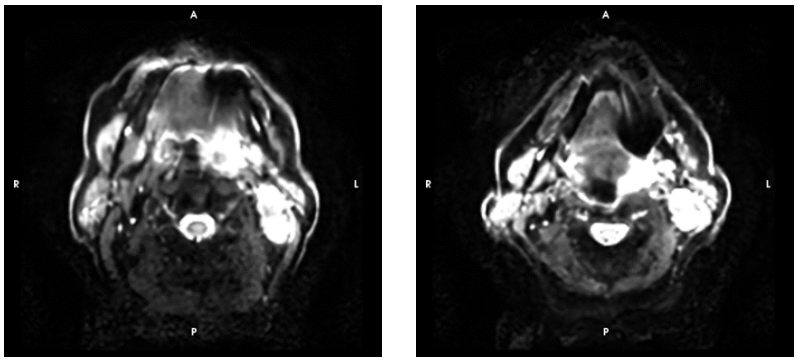

Figure 22: ssEPI, uncorrected $b = 0$ images of patient 1 in directions AP (left) and PA (right).

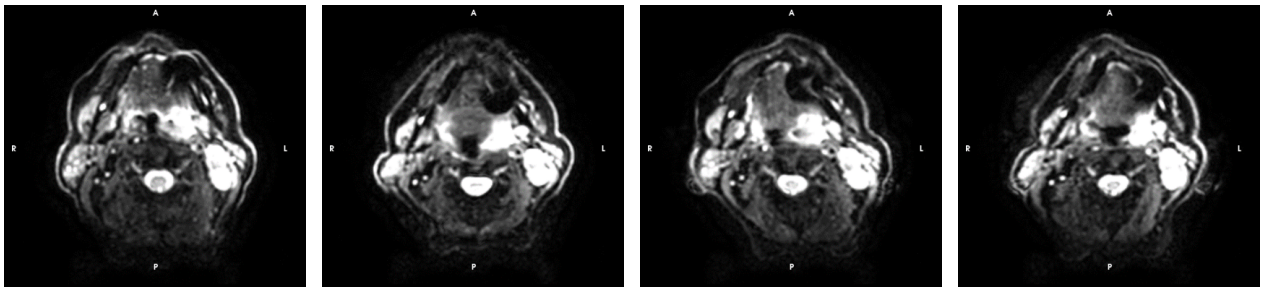

Figure 23: MUSE, uncorrected $b0$ images of patient 1 in directions AP, PA, RL, and LR from left to right.

The two corrected images (Fig. 24) are very similar and seem to agree well with the T2w image. Certain areas differ between the images, such as around the dental implant, and the tip of the chin, in which case MUSE provides a better basis for correction and thereby yields better results.

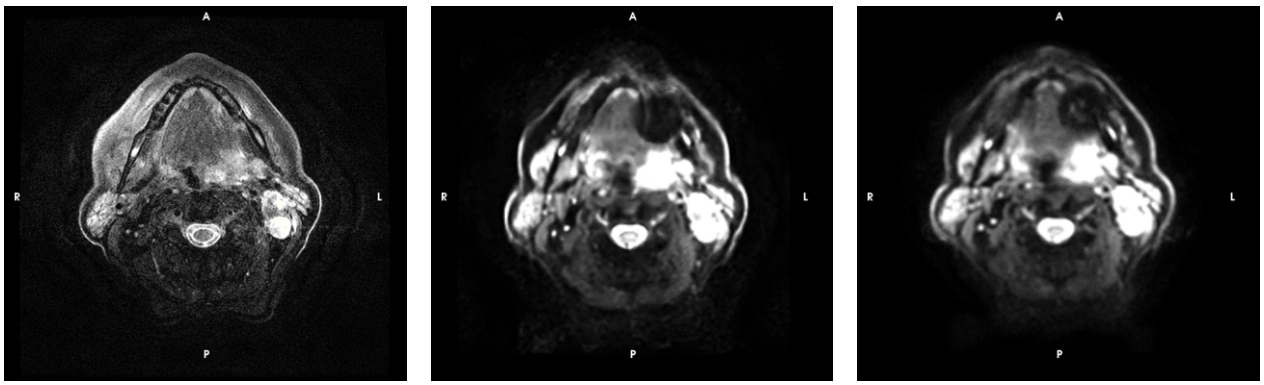

Figure 24: Patient 1, $b = 0$ images. T2w image (left), corrected ssEPI with directions AP/PA, corrected MUSE with all four directions. Note that the patient has dental implants which appear as dark circles along the jaw. The primary tumour lies left along the pharynx, and an affected lymph lies aside it.

The tumour lies in a similar area for for patient 2 (Fig. 25). This patient was scanned with a fixation mask, which is slightly visible along the body contour in the diffusion images. The area of the tumour which lies close to the pharynx is different in the two images. Again, the MUSE has corrected the shape in this area better, and aligns more with that of the T2w image.

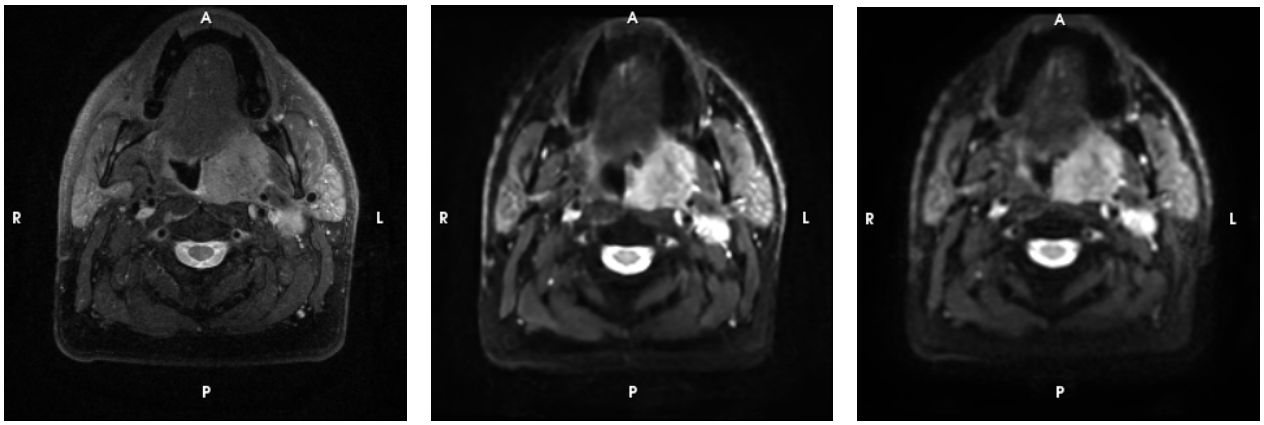

Figure 25: Patient 2, $b = 0$ images. T2w image (left), corrected ssEPI with directions AP/PA (middle), corrected MUSE with all four directions (right). Note that the patient has dental implants which appear as dark circles along the jaw. The primary tumour lies left along the pharynx, and an affected lymph lies aside it.

Fig. 26 and Fig. 27 show the parameter maps (f, D) and the resultant hypoxia map for patient 1 and 2 respectively. Visually there are obvious differences between the parameter maps for the two sequences, particularly notable in the f-map. The inconsistency between ssEPI and MUSE is less apparent for patient 2, where the two hypoxia maps agree well.

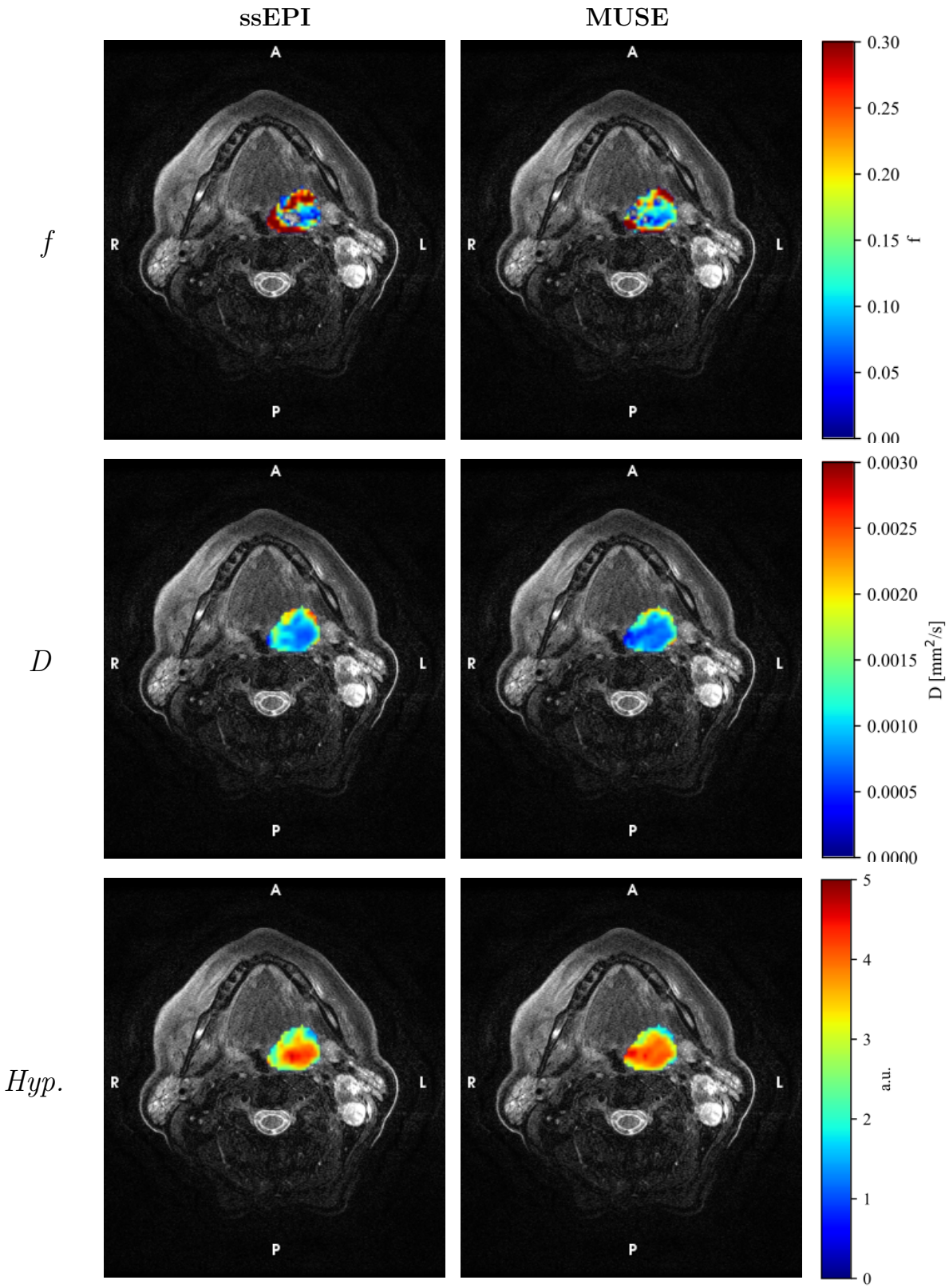

Figure 26: Patient 1. IVIM mapping of parameters f and D (top and middle row respectively), and a hypoxia map based on Hompland et al. (bottom row) calculated from ssEPI images (left column) and MUSE images (right column) [12]. The f-map is windowed between $0 - 0.3$, and D is windowed between $0 - 0.3 \cdot 10^{-2}$ mm^2/s. The hypoxia map is arbitrary, red implies more hypoxic areas.

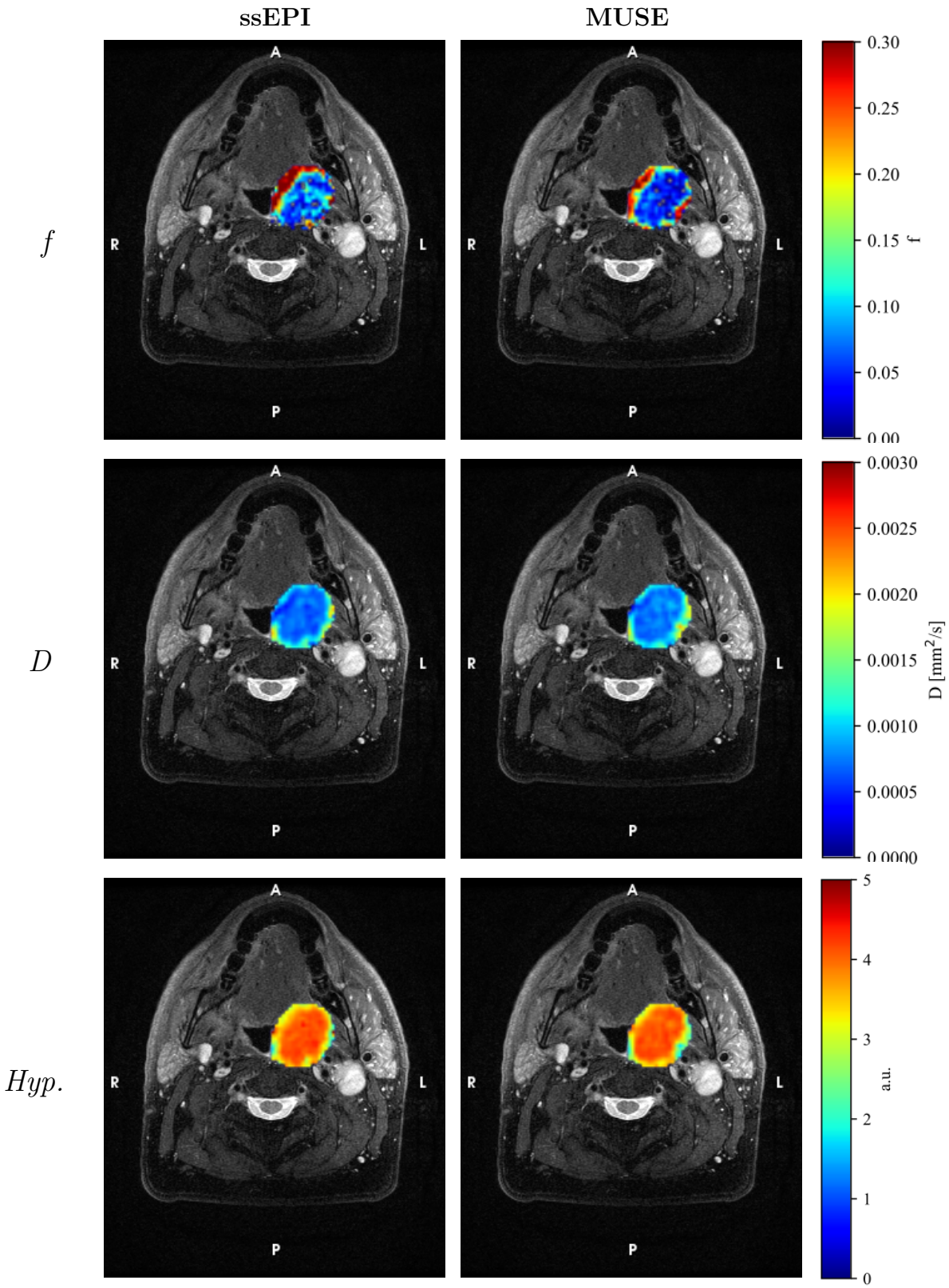

Figure 27: Patient 2. IVIM mapping of parameters f and D (top and middle row respectively), and a hypoxia map based on Hompland et al. (bottom row) calculated from ssEPI images (left column) and MUSE images (right column) [12]. The f-map is windowed between $0 - 0.3$, and D is windowed between $0 - 0.3 \cdot 10^{-2}$ mm^2/s. The hypoxia map is arbitrary, red implies more hypoxic areas.

5 Discussion

5.1 Phantom images

The ssEPI images show severe distortion near the interfaces around and inside the phantom (Fig. 9). The structure in the centre of the oval depicting the tilted test-tube, which is supposed to appear in the shape of an oval, has been badly deformed in particular. The central oval is stretched into a U-shape along the phase encoding direction, seen most clearly in the ssEPI images. Surrounding the oval, notable signal accumulation or pile-up occurs, primarily at the bottom and top of the U-shape. For example, in the AP phase encoding direction, pile-up accumulates on the posterior side of the oval's centre (under the bottom of the U) and on the anterior of its sides (over the top of the U). The increased distortion compared to the circle is likely attributed to slice thickness in conjunction with the tilted test tube. While reducing slice thickness may mitigate this issue, it could compromise SNR, posing practical constraints.

Previous studies have shown that MUSE sequences provide higher image quality with milder distortions, and better lesion detectibility [42, 58]. In agreement with these studies, the results of this work shows MUSE to produce images with less distortions and higher geometric accuracy (Fig. 10). The result of the distortion corrections depend on both sequence and the phase encoding directions used. Areas with pile-up are hard to correct for, this can be seen most clearly in the vendor-correction. Out of all four types of corrections (Fig. 11), the vendor image shows the least improvement. The areas around the central oval are not homogeneous and the pileup is prominent. The sequence intended for the embedded vendor-based correction only acquires one additional b0 volume with the reverse phase encoding direction and corrects the entire set based on that single volume. Thus, the correction algorithm incorporates less information, resulting in a coarser correction. This is true for both sequences, however, as the MUSE sequence (Fig. 12) has less severe distortions, the vendor based corrected image has less obvious areas of pile-up and signal inhomogeneity compared to the ssEPI. The images also show a difference between the phase encoding direction pairs AP/PA and RL/LR in the way that the pile-up gets distributed by the correction. Specifically for ssEPI, the distortions cause the central oval to curve into itself. This means that in both images with opposite phase encoding polarity there is signal in what should be the centre of the oval. This overlap is not corrected well, as is seen all the ssEPI corrected images, appearing as signal in the centre of the oval (Fig. 11d). This appears in corrections with all phase encoding directions, but is particularly prominent in the AP/PA direction. This issue is not present for the MUSE images, most likely because the distorted curve of the oval is not as pronounced. Furthermore, this issue only appears in the centre oval, and is not an issue for the circle above it. This means that depending on the image itself and its geometry, corrections in certain directions can be preferable. The performance of the four direction correction is difficult to discern visually, especially for the ssEPI image.

The quantitative evaluation indicates that corrections of ssEPI have the possibility to be accurate, and improve the geometric accuracy by a considerable amount (Fig. 13, 15). By the metric used for these figures, all corrected ssEPI images, including the vendor-based corrections, are more geometrically accurate than the original uncorrected MUSE image.

Out of all images, MUSE corrected in AP/PA seems to yield the best results (Fig. 14, 16). However, while the correction of MUSE in RL/LR is less accurate than the AP/PA, the opposite is true for ssEPI, where RL/LR indicate a higher agreement to the T2w image. This could be attributed to the method used for the generation of the volumes investigated. The volumes where generated through thresholding, which is problematic when the edges of structures are diffuse. In particular, the oval in the centre of the phantom has diffuse edges compared the the other structures. Furthermore, the discrepancy of the superior phase encoding direction could be due to the geometry of the imaged object, in combination with the phase encoding direction, and the extent of the distortions. This would indicate that the direction which the oval lies in relation the the phase encoding directions (e.g. along the phase encoding direction such as the RL/LR image, or against the phase encoding direction such as the AP/PA image) affect the result. By extension, this indicates that the correction is dependent on patient geometry. The MUSE corrected in all four directions performed the next best. These images imply that a ssEPI sequence should perhaps only be used when the phase encoding direction is along the major axis of any cavity. In a patient this might mean that in order to image the mouth and sinuses using ssEPI, the phase encoding directions should be AP/PA. The corrections in four directions have the advantage of being invariant to the geometry of the object being imaged, and could therefore be a preferable alternative to circumvent these issues.

The impact of background gradients on diffusion encoding is evident (Fig. 17). The apparent diffusion coefficient (ADC) calculated along three axes (x, y, z) reveals signal misplacement characterised by bright and dark regions which should otherwise be homogeneous. Notably, a bright strip along the outer contour appears on the posterior edge of the phantom, and similarly, a dark strip appears along the anterior edge. Signal misplacement also occurs within distorted areas of the phantom. Specifically, within the oval, lighter regions show at the top and along the inner curvature of the U-shape. However, the ADC image derived from opposite polarity pairs (x, -x, y, -y, z, -z) show, aside from geometric distortions, greater homogeneity. Signal misplacement along the phantom's outer contours is less pronounced, and susceptibility differences have a reduced impact on the areas surrounding the U-shape and the calculated ADC. Incorporating the mean of opposite polarity diffusion gradients in the analysis mitigates these issues, albeit at the expense of acquiring three additional images, and more image processing steps. The result might not be compatible with the manufacturer's ADC calculation thereby rendering it unsuitable for routine patient examinations. When interpreting in-vivo results, it is essential to consider the high uncertainty associated with signal from areas surrounding interfaces. However, compensating for these effects is outside the scope of this project and was not incorporated in the in-vivo imaging. Rather it should be regarded as a future prospect to potentially further improve the dMRI image quality.

5.2 In-vivo Images

5.2.1 Healty Volunteer Images

The in vivo images taken with the original sequence were highly distorted, making anatomical features difficult to discern (Fig. 18). The most severe distortions occur in the anterior region, particularly the face. The posterior region, with fewer air-tissue interfaces, is less affected

but still visibly distorted. The entire structures appear stretched in the phase encoding direction, resulting in poor image quality. There is signal from outside the body contour that has become separated, resembling a ghosting artefact. Additionally, there are areas with noticeable signal pile-up, rendering the anatomy indistinguishable. In the AP and PA directions, the body appears stretched or compressed, respectively, further contributing to severe distortions. Despite these issues, some areas such as the tongue remain vaguely discernible in the AP and PA directions. The images obtained using the final method show clear improvement compared to the initial images (Fig. 19). General distortions are reduced, and each image is less stretched in the phase encoding direction. When comparing the MUSE and ssEPI images, the difference is less pronounced than in the phantom images, although the body in the MUSE images is less stretched or slanted. A large contributor of the improved image quality is likely the enhanced fat saturation. Due to the limited bandwidth in the phase encoding direction, EPI sequences are also sensitive towards chemical shift artefacts and are as standard run with fat-suppression [7]. Thus, the enhanced suppression reduced the signal displacement of fat-containing tissues and provided better grounds for the correction.

The three corrected in-vivo images show seemingly little difference between them (Fig. 19f, 19g, 19h). The main difference is observed along the tongue and in the pharynx. The tongue in the ssEPI AP/PA image has signal loss along the centre, and is less homogeneous when compared to the tongues in the other corrected images. Furthermore, the pharynx, as shown in the T2w image, is quite small compared to in the diffusion images. Both the corrections in four directions do well in correcting this area. The ssEPI in AP/PA succeeded the least in correcting this area, the air pocket is larger in the AP/PA image compared to the other images. Thus, using four phase encoding directions to correct directly around air cavities is superior. Between the ssEPI and MUSE in four directions, it is harder to discern which correction is superior, since both seem to have high geometric accuracy. The MUSE sequence has the advantage of a lesser distorted original image, which means that fewer uncertainties are introduced by the correction. Disregarding the possible motion-induced inaccuracies that multi-shot sequences tend to be sensitive to, there is no clear distortion-related advantage of choosing a four directional ssEPI over MUSE. During the optimisation process of the in-vivo sequences, it was noted that corrections based solely on phase encoding in RL/LR produced results inferior to those of AP/PA, it was therefore not included as an alternative in the final protocol. Between the two ssEPI images, the correction in AP/PA is less blurry and edges of contours are more defined (Fig. 19f, 19g). Details around the posterior of the bosy are more discernible. This is likely due to the contribution of RL/LR in the four direction correction. Between the two ssEPI images, the AP/PA corrections could be an option when sharp images are a priority. Although the distortion is less extensive in the MUSE images, multi-shot sequences tend to have other issues due to e.g. movement artefacts. The signal should be validated quantitatively prior to wider implementation, as inaccuracies caused by movements between the shots in the image is common. Previous studies have reported similar ADC values between ssEPI and MUSE, with no significant difference [58, 59]. Regardless, this is an aspect to consider when choosing a sequence for quantitative analysis.

The maximum displacement (Fig. 20) in the ssEPI images is several millimetres larger than that in the MUSE images, specifically 12 mm versus 8 mm, respectively. The regions with

high displacements are also more extensive, particularly around the jaw. The correction around the pharynx in the MUSE images is more apparent, appearing as a brighter ring in the centre of the body. There is a difference in SNR between the two sequences, as illustrated in Fig. 21, with the b=800 image for MUSE appearing noisier. This discrepancy is likely not inherent to the sequence itself but rather a consequence of the vendor software. Notably, an SNR improvement algorithm was applied for the ssEPI but not for MUSE. Therefore, the SNR of the sequences is not comparable in these results. However, newer versions of the vendor software offer this option for MUSE as well. In order to draw any general conclusions concerning the SNR of the sequences they need to be run with the same conditions.

5.2.2 Patient Images and IVIM Analysis

The patient images are corrected in a manner similar to the images of the healthy volunteer, using ssEPI in AP/PA and four directional MUSE. Between the two corrected images for patient 1, there is a slight difference in the shape of the tumour tissue, but the corrections have otherwise performed well. The results are more easily distinguished in the mapping of IVIM parameters f and D, and the hypoxia map. Comparing f for patient 1 (Fig. 26), the areas in ssEPI have higer values along the edges of the tumour, as indicated by the darker red on the anterior and right side of the body. Comparatively, the MUSE f-map has larger mid-range areas indicated by the blue and green. Both the D map and the resulting Hypoxia map differs between the sequences as well. The low values for f and D (blue) correspond to high cell density and low micro-circulation indicating hypoxic areas. The generated hypoxia map has been set to an arbitrary unit, as values are calculated relative each other [12]. For patient 1 (Fig. 26) the hypoxia map differs considerably between the two sequences, where the ssEPI has high values contained in a smaller area in the centre off the structure, and MUSE has higher values extending to the anterior and right side of the tumour, towards the pharynx. The reason for the discrepancy between sequences is unclear, but could be attributed to any of the aforementioned differences between them, such as the distortions and corrections, or noise. As previously discussed, the area around the pharynx is subject to large distortions, and signal is displaced accordingly by the correction. It is possible that the MUSE sequence, due to less distortions in the original images, better indicate the hypoxic areas close to tissue-air interfaces. The hypoxia map for patient 2 (Fig. 27) is more similar between sequences, but visible differences in the parameter maps, particularly f can be observed, where the anterior of the tumour has a higher perfusion fraction for ssEPI. There is no conclusion that can be drawn from this sample size. Regardless, it is possible that either sequence could provide images that while not precise, give indication of hypoxic and normoxic areas. Ideally, these results would be compared to similar studies or already validated methods of hypoxia mapping. However, as there is no currently available H&N hypoxia data comparing this method to e.g. histology, there is no way to validate the results of this study or conclude which sequence yield more accurate results. It is difficult to recommend MUSE, as while neither has been validated in this study, ssEPI is considered the standard. Furthermore, the hypoxia mapping method was developed for prostate and validated against prostate histology using pimonidazole. The distribution of parameter values in prostate and H&N tumours may not be identical, which affects the hypoxia estimation. These results show that a similar model can be applied, however the accuracy of the results

cannot be further discussed due to the inherent uncertainties in the calculation of the hypoxia map.

5.3 Limitations and Future Prospects

Several limitations were encountered during this project, which have implications for the reliability and applicability of the results. Firstly, the MRI camera used in this study had a relatively low peak gradient amplitude and slew rate. This limitation significantly impacts the echo time, which in this case was 71 ms, leading to signal loss. Utilising a camera with superior hardware, capable of lower echo times would likely have resulted in higher image quality. The magnetic field strength was also 3 T, which contributes to the larger distortions. Furthermore, the constraints of radiotherapy setup limits the choice of coils to those compatible with a fixation mask, which are generally less optimal than a standard head and neck coil in terms of SNR. It is plausible that using a standard coil could have produced images with higher SNR, thereby enhancing image quality.

The manual data processing is another limitation in terms of the applications of the project. The use of various software programs made the process somewhat tedious and difficult to reproduce, reducing user-friendliness. Future work could benefit from more streamlined and automated processing techniques to enhance reproducibility and ease of use.

There are also considerable uncertainties associated with the quantitative IVIM parameters obtained. Factors such as the diffusion signal from MUSE, potential motion-based interference like swallowing artefacts, background gradient effects (such as those described in section 5.1), choice of b-values, selection of the simplified IVIM model, and the calculation and translation of hypoxia maps from prostate to head and neck have not been fully validated. Before implementing this method clinically, these factors would need thorough validation, ideally against histology or other reliable methods.

Additionally, the study's sample size was small, with only two patients scanned using the method. This small sample size limits the ability to draw generalise conclusions. Expanding the sample size in future studies would be essential to establish the robustness and reliability of the findings.

Despite these limitations, there are promising avenues for improvement. Advances in MRI hardware, such as cameras with higher peak gradient amplitudes and faster slew rates, could reduce distortions. Furthermore, continued research and validation of quantitative IVIM parameters and hypoxia mapping against reliable benchmarks could establish a clinically useful method for hypoxia mapping in the H&N region. Moving forward, these improvements hold the potential for significant advancements in the application of quantitative diffusion MRI in radiotherapy.

6 Conclusion

This project aimed to evaluate various distortion correction techniques for dMRI in the H&N region, with a focus on improving geometric accuracy for the development of imaging

biomarkers for radiotherapy planning. Susceptibility artifacts and correction methods for ssEPI and MUSE sequences with various phase encoding directions were evaluated. While both sequences can yield satisfactory results, MUSE generally exhibits fewer susceptibility-related distortions, leading to better correction outcomes. Conversely, ssEPI images tend to show more significant geometric distortions. Furthermore, the corrected ssEPI images show improved geometric accuracy comparable to the corrected MUSE images.

In-vivo imaging results further support MUSE sampling causing less profound distortions. However, using correction methods, ssEPI AP/PA images gain improved geometric accuracy and could compete with corrected MUSE images. Looking solely at geometric distortions, MUSE is the superior sequence. However, in IVIM analysis, the two sequences produce dissimilar parameter maps which can affect subsequent imaging biomarkers. The diffusion signal needs to be validated in order to be able to recommend one sequence over the other.

Overall, this study shows the importance of sequence selection and distortion correction in minimising susceptibility artifacts and optimising image quality. While MUSE sequences offer substantial advantages, considerations regarding motion artifacts are crucial. Future efforts should focus on enhance the reliability and accuracy of the results. In summary, despite challenges, there is potential for advancing dMRI techniques in H&N for radiotherapy. With ongoing improvements and research, more accurate and clinically useful imaging protocols are promising.

Acknowledgements

I have many people to thank for supporting me during this project. First and foremost, thank you to all my supervisors; Minna Lerner, Ivan A. Rashid, Gabriel Adrian, Lars E. Olsson, and Patrik Brynolfsson, for all your help and input to this project. Thank you for the time and effort you've spent in trying to make this thesis as fun as it has been. I would like to give a special thank you to my main supervisor, Minna, for always looking after me and having my back. Thank you for making sure I have my opinions heard and don't get overwhelmed during a generally overwhelming process. There have been several instances during these months where I have found myself exceedingly grateful for your guidance and support. I would like to thank Patrik, for always having the answer to any and every question I could possibly ask. Whenever I am stuck or have an issue you have always been ready to help at a moments notice. I would like to thank Ivan, for being so invested in my project, and always finding new ideas for me to explore. Lastly, I would like to thank Leo, for always looking after my best interests and my future prospects.

I would also like to thank my family—my parents and brother. Even though you don't always understand what I'm talking about, you always listen patiently when I'm yapping about whatever happens to be on my mind at the moment. Thank you for letting me ramble, and thank you for always showing that you are proud of me. Lastly, thank you to my classmates for these last three years together. Thank you for all the hangman and all the card games we've played, and thank you for the lovely company during stressful times. Thank you specifically to my fellow dMRI thesis buddies, Julia and Felix. I would not have managed through these months without our frequent crisis meetings to keep me sane.
Sincerely,

Thank you.

References

1. Jones DK. Diffusion MRI: Theory, Methods, and Applications. Oxford, New York: Oxford University Press, 2010.
2. Olsson LE, Johansson M, Zackrisson B, Blomqvist LK. Basic concepts and applications of functional magnetic resonance imaging for radiotherapy of prostate cancer. Phys Imaging Radiat Oncol 2019;9:50–7.
3. Lund University Hospital. ARTSCAN VI Protocol Version 1, 2023-07-03 ARTSCAN VI - a Multicentre Phase III Study of Risk-based Treatment Intensification With Hyperfractionated Radiotherapy in Head and Neck Cancer Patients [Internet]. Clinical trial registration NCT06248996. submitted: January 31, 2024. Lund, Sweden, 2024. URL: `https://clinicaltrials.gov/study/NCT06248996` [cited 01/01/2024].
4. Schakel T, Hoogduin JM, Terhaard CH, Philippens ME. Technical Note: Diffusion-weighted MRI with minimal distortion in head-and-neck radiotherapy using a turbo spin echo acquisition method. Med. Phys. 2017;44(8):4188–93.
5. Ding Y, Meheissen MAM, Zhou K, Mohamed ASR, Wen Z, Ng SP, et al. Evaluation of different diffusion-weighted image techniques for head and neck radiation treatment: phantom and volunteer studies. medRxiv [preprint] 2022.
6. Le Bihan D, Poupon C, Amadon A, Lethimonnier F. Artifacts and pitfalls in diffusion MRI. J. Magn. Reson. Imaging 2006;24(3):478–88.
7. McRobbie DW, Moore EA, Graves MJ, Prince MR, eds. Acronyms Anonymous I: Spin Echo. In: MRI from Picture to Proton. 3rd ed. Cambridge: Cambridge University Press, 2017. Chap. 12:185–206.
8. Gaeta M, Cavallaro M, Vinci SL, Mormina E, Blandino A, Marino MA, et al. Magnetism of materials: theory and practice in magnetic resonance imaging. Insights Imaging 2021;12(1):179.
9. Jensen K, Al-Farra G, Dejanovic D, Eriksen JG, Loft A, Hansen CR, et al. Imaging for Target Delineation in Head and Neck Cancer Radiotherapy. Semin Nucl Med 2021;51(1):59–67.
10. Owrangi AM, Greer PB, Glide-Hurst CK. MRI-only treatment planning: benefits and challenges. Phys Med Biol 2018;63(5):05TR01.
11. Gunnlaugsson A, Persson E, Gustafsson C, Kjellén E, Ambolt P, Engelholm S, et al. Target definition in radiotherapy of prostate cancer using magnetic resonance imaging only workflow. Phys Imaging Radiat Oncol 2019;9:89–91.
12. Hompland T, Hole KH, Ragnum HB, Aarnes EK, Vlatkovic L, Lie AK, et al. Combined MR Imaging of Oxygen Consumption and Supply Reveals Tumor Hypoxia and Aggressiveness in Prostate Cancer Patients. Cancer Res. 2018;78(16):4774–85.
13. Tax CMW, Bastiani M, Veraart J, Garyfallidis E, Okan Irfanoglu M. What's new and what's next in diffusion MRI preprocessing. NeuroImage 2022;249:118830.

14. Chen Nk, Guidon A, Chang HC, Song AW. A robust multi-shot scan strategy for high-resolution diffusion weighted MRI enabled by multiplexed sensitivity-encoding (MUSE). Neuroimage 2013;72:41–7.

15. Andersson JLR, Skare S, Ashburner J. How to correct susceptibility distortions in spin-echo echo-planar images: application to diffusion tensor imaging. NeuroImage 2003;20(2):870–88.

16. Smith SM, Jenkinson M, Woolrich MW, Beckmann CF, Behrens TEJ, Johansen-Berg H, et al. Advances in functional and structural MR image analysis and implementation as FSL. Neuroimage 2004;23 Suppl 1:S208–219.

17. Hill RM, Rocha S, Parsons JL. Overcoming the Impact of Hypoxia in Driving Radiotherapy Resistance in Head and Neck Squamous Cell Carcinoma. Cancers (Basel) 2022;14(17):4130.

18. Krock BL, Skuli N, Simon MC. Hypoxia-Induced Angiogenesis. Genes Cancer 2011;2(12):1117–33.

19. Hall EJ, Giaccia AJ. Radiobiology for the Radiologist. 6th ed. Philadelphia, USA: Lippincott Williams & Wilkins, 2006.

20. Beckers C, Pruschy M, Vetrugno I. Tumor hypoxia and radiotherapy: A major driver of resistance even for novel radiotherapy modalities. Semin Cancer Biol. 2024;98:19–30.

21. Boulefour W, Rowinski E, Louati S, Sotton S, Wozny AS, Moreno-Acosta P, et al. A Review of the Role of Hypoxia in Radioresistance in Cancer Therapy. Med Sci Monit 2021;27:e934116–1–e934116–7.

22. Wang H, Jiang H, Van De Gucht M, De Ridder M. Hypoxic Radioresistance: Can ROS Be the Key to Overcome It? Cancers (Basel) 2019;11(1):112.

23. Gérard M, Corroyer-Dulmont A, Lesueur P, Collet S, Chérel M, Bourgeois M, et al. Hypoxia Imaging and Adaptive Radiotherapy: A State-of-the-Art Approach in the Management of Glioma. Front. Med. 2019;6.

24. Li JZ, Gao W, Chan JYW, Ho WK, Wong TS. Hypoxia in head and neck squamous cell carcinoma. ISRN Otolaryngol 2012;2012:708974.

25. Bredell MG, Ernst J, El-Kochairi I, Dahlem Y, Ikenberg K, Schumann DM. Current relevance of hypoxia in head and neck cancer. Oncotarget 2016;7(31):50781–804.

26. Le QT, Courter D. Clinical Biomarkers for Hypoxia Targeting. Cancer Metastasis Rev 2008;27(3):351–62.

27. Wiedenmann N, Grosu AL, Büchert M, Rischke HC, Ruf J, Bielak L, et al. The utility of multiparametric MRI to characterize hypoxic tumor subvolumes in comparison to FMISO PET/CT. Consequences for diagnosis and chemoradiation treatment planning in head and neck cancer. Radiother Oncol 2020;150:128–35.

28. O'Connor JPB, Boult JKR, Jamin Y, Babur M, Finegan KG, Williams KJ, et al. Oxygen-Enhanced MRI Accurately Identifies, Quantifies, and Maps Tumor Hypoxia in Preclinical Cancer Models. Cancer Res 2016;76(4):787–95.

29. Salem A, Little RA, Latif A, Featherstone AK, Babur M, Peset I, et al. Oxygen-enhanced MRI Is Feasible, Repeatable, and Detects Radiotherapy-induced Change in Hypoxia in Xenograft Models and in Patients with Non-small Cell Lung Cancer. Clin Cancer Res 2019;25(13):3818–29.

30. O'Connor JPB, Robinson SP, Waterton JC. Imaging tumour hypoxia with oxygen-enhanced MRI and BOLD MRI. Br J Radiol 2019;92(1096):20180642.

31. Gaustad JV, Hauge A, Wegner CS, Simonsen TG, Lund KV, Hansem LMK, et al. DCE-MRI of Tumor Hypoxia and Hypoxia-Associated Aggressiveness. Cancers (Basel) 2020;12(7):1979.

32. Gulliksrud K, Øvrebø KM, Mathiesen B, Rofstad EK. Differentiation between hypoxic and non-hypoxic experimental tumors by dynamic contrast-enhanced magnetic resonance imaging. Radiotherapy and Oncology 2011;98(3):360–4.

33. Biggers A. What to know about MRI contrast side effects [Internet]. Medical News Today. 2023. URL: https://www.medicalnewstoday.com/articles/mri-contrast-side-effects [cited 04/01/2024].

34. Kanda T, Ishii K, Kawaguchi H, Kitajima K, Takenaka D. High signal intensity in the dentate nucleus and globus pallidus on unenhanced T1-weighted MR images: relationship with increasing cumulative dose of a gadolinium-based contrast material. Radiology 2014;270(3):834–41.

35. Iima M. Perfusion-driven Intravoxel Incoherent Motion (IVIM) MRI in Oncology: Applications, Challenges, and Future Trends. Magn Reson Med Sci 2021;20(2):125–38.

36. Campbell JSW, Bruce Pike G. Diffusion Magnetic Resonance Imaging. In: Encyclopedia of Biomedical Engineering. Ed. by Narayan R. Oxford: Elsevier, 2019:505–18.

37. White NS, McDonald C, Farid N, Kuperman J, Karow D, Schenker-Ahmed NM, et al. Diffusion-weighted imaging in cancer: Physical foundations and applications of Restriction Spectrum Imaging. Cancer Res 2014;74(17):4638–52.

38. Mohammadi S, Hutton C, Nagy Z, Josephs O, Weiskopf N. Retrospective Correction of Physiological Noise in DTI Using an Extended Tensor Model and Peripheral Measurements. Magn. Reson. Med. 2013;70.

39. Clare S. Functional MRI : Methods and Applications. [dissertation]. University of Nottingham, 1997. URL: https://www.semanticscholar.org/paper/Functional-MRI-%3A-Methods-and-Applications-Clare/92a00b61d1489607a34858181694817fff1dc06d [cited 05/10/2024].

40. Miller KL. Diffusion Acquisition: Pushing the Boundaries. In: Diffusion MRI. Ed. by Johansen-Berg H, Behrens TEJ. 2nd ed. San Diego: Academic Press, 2014. Chap. 3:35–61.

41. Gallichan D, Andersson JLR, Jenkinson M, Robson MD, Miller KL. Reducing distortions in diffusion-weighted echo planar imaging with a dual-echo blip-reversed sequence. Magn Reson Med. 2010;64(2):382–90.

42. Kim YY, Kim MJ, Gho SM, Seo N. Comparison of multiplexed sensitivity encoding and single-shot echo-planar imaging for diffusion-weighted imaging of the liver. Eur. J. Radiol. 2020;132:109292.

43. Cai J, Wang L, Wu P, Li Z, Tong L, Sun S. Study on oxygen enrichment from air by application of the gradient magnetic field. J. Magn. Magn. Mater. 2008;320(3):171–81.

44. Klohs J, Hirt AM. Investigation of the magnetic susceptibility properties of fresh and fixed mouse heart, liver, skeletal muscle and brain tissue. Physica Medica 2021;88:37–44.

45. Farahani K, Sinha U, Sinha S, Chiu LCL, Lufkin RB. Effect of field strength on susceptibility artifacts in magnetic resonance imaging. Comput. Med. Imaging Graph 1990;14(6):409–13.

46. Begnoche JP, Schilling KG, Boyd BD, Cai LY, Taylor WD, Landman BA. EPI susceptibility correction introduces significant differences far from local areas of high distortion. Magn. Reson. Imaging 2022;92:1–9.

47. Le Bihan D. What can we see with IVIM MRI? Neuroimage 2019;187:56–67.

48. Le Bihan D, Iima M, Federau C, Sigmund EE, eds. Intravoxel incoherent motion (IVIM) MRI: principles and applications. Singapore: Pan Stanford Publishing, 2019. 533 pp.

49. Szubert-Franczak AE, Naduk-Ostrowska M, Pasicz K, Podgórska J, Skrzyński W, Cieszanowski A. Intravoxel incoherent motion magnetic resonance imaging: basic principles and clinical applications. Pol J Radiol 2020;85:e624–e635.

50. Noij DP, Martens RM, Marcus JT, Bree R de, Leemans CR, Castelijns JA, et al. Intravoxel incoherent motion magnetic resonance imaging in head and neck cancer: A systematic review of the diagnostic and prognostic value. Oral Oncol. 2017;68:81–91.

51. Duan Z, Tao J, Liu W, Liu Y, Fang S, Yang Y, et al. Correlation of IVIM/DKI Parameters with Hypoxia Biomarkers in Fibrosarcoma Murine Models: Direct Control of MRI and Pathological Sections. Acad. Radiol. 2024;31(3):1014–23.

52. Mo T, Brandal SHB, Köhn-Luque A, Engebraaten O, Kristensen VN, Fleischer T, et al. Quantification of Tumor Hypoxia through Unsupervised Modelling of Consumption and Supply Hypoxia MR Imaging in Breast Cancer. Cancers (Basel) 2022;14(5):1326.

53. Rydhög AS, Osch MJP van, Lindgren E, Nilsson M, Lätt J, Ståhlberg F, et al. Intravoxel incoherent motion (IVIM) imaging at different magnetic field strengths: What is feasible? Magn. Reson. Imaging 2014;32(10):1247–58.

54. Yang L, Wu X, Wang Y, Shi G, Hu H, Duan X. Comparison of image quality and quantitative parameters in intravoxel incoherent motion imaging at 3-T based on turbo spin-echo and echo-planar imaging in patients with oral cancer. Diagn Interv Radiol 2023;29(6):786–93.

55. Szczepankiewicz F, Sjölund J. Cross-term-compensated gradient waveform design for tensor-valued diffusion MRI. J. Magn. Reson. 2021;328:106991.

56. Neeman M, Freyer JP, Sillerud LO. A simple method for obtaining cross-term-free images for diffusion anisotropy studies in NMR microimaging. Magn Reson Med 1991;21(1):138–43.

57. Klein S, Staring M, Murphy K, Viergever MA, Pluim JPW. elastix: a toolbox for intensity-based medical image registration. IEEE Trans Med Imaging 2010;29(1):196–205.

58. Konar AS, Fung M, Paudyal R, Oh JH, Mazaheri Y, Hatzoglou V, et al. Diffusion-Weighted Echo Planar Imaging using MUltiplexed Sensitivity Encoding and Reverse Polarity Gradient in Head and Neck Cancer: An Initial Study. Tomography 2020;6(2):231–40.

59. Zhao W, Ju S, Yang H, Wang Q, Fang L, Pylypenko D, et al. Improved Value of Multiplexed Sensitivity Encoding DWI with Reversed Polarity Gradients in Diagnosing Prostate Cancer: A Comparison Study with Single-Shot DWI and MUSE DWI. Acad. Radiol. 2023.